

ornl

ORNL/TM-11887

**OAK RIDGE
NATIONAL
LABORATORY**

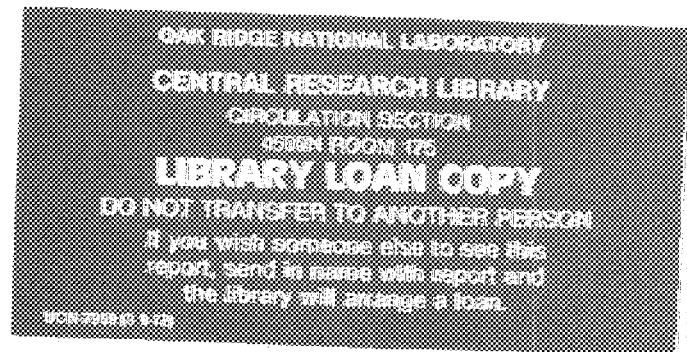
MARTIN MARIETTA



3 4456 0364275 2

The Oxidation of Type 310S Stainless Steel in Mixed Gases at Elevated Temperatures

J. S. Wolf
O. B. Cavin
J. H. DeVan



MANAGED BY
MARTIN MARIETTA ENERGY SYSTEMS, INC.
FOR THE UNITED STATES
DEPARTMENT OF ENERGY

This report has been reproduced directly from the best available copy.

Available to DOE and DOE contractors from the Office of Scientific and Technical Information, P.O. Box 62, Oak Ridge, TN 37831; prices available from (615) 576-8401, FTS 626-8401.

Available to the public from the National Technical Information Service, U.S. Department of Commerce, 5285 Port Royal Rd., Springfield, VA 22161.

This report was prepared as an account of work sponsored by an agency of the United States Government. Neither the United States Government nor any agency thereof, nor any of their employees, makes any warranty, express or implied, or assumes any legal liability or responsibility for the accuracy, completeness, or usefulness of any information, apparatus, product, or process disclosed, or represents that its use would not infringe privately owned rights. Reference herein to any specific commercial product, process, or service by trade name, trademark, manufacturer, or otherwise, does not necessarily constitute or imply its endorsement, recommendation, or favoring by the United States Government or any agency thereof. The views and opinions of authors expressed herein do not necessarily state or reflect those of the United States Government or any agency thereof.

ORNL/TM-11887

Metals and Ceramics Division

THE OXIDATION OF TYPE 310S STAINLESS STEEL
IN MIXED GASES AT ELEVATED TEMPERATURES

J. S. Wolf
O. B. Cavin
J. H. DeVan

Date Published: April 1992

Prepared for the
DOE Office of Transportation Systems
EE 06 00 00 0

Prepared by the
OAK RIDGE NATIONAL LABORATORY
Oak Ridge, Tennessee 37831-6285
managed by
MARTIN MARIETTA ENERGY SYSTEMS, INC.
for the
U.S. DEPARTMENT OF ENERGY
under contract DE-AC05-84OR21400



3 4456 0364275 2

CONTENTS

	<u>Page</u>
LIST OF TABLES	v
LIST OF FIGURES	vii
ABSTRACT	1
1. INTRODUCTION	2
2. PROCEDURE	3
2.1 MATERIALS	3
2.2 SPECIMEN DESIGN	4
2.3 SPECIMEN PREPARATION	5
2.4 EXPOSURE APPARATUS	7
2.5 SPECIMEN EXPOSURES	11
2.6 ANALYTICAL METHODS	14
2.6.1 Mass and Dimensional Changes	15
2.6.2 Metallography	15
2.6.3 SEM and EDS	15
2.6.4 X-ray Diffraction	16
3. RESULTS	17
3.1 PRELIMINARY TESTS	18
3.2 BASELINE OXIDATION IN AIR	27
3.3 "LEAN" SULFIDIZING ATMOSPHERES	39
3.4 "RICH" SULFIDIZING ATMOSPHERES	50
4. DISCUSSION	62
4.1 THERMOCHEMICAL CONSIDERATIONS	62
4.2 DEFORMATION CONSIDERATIONS	65
4.3 STRUCTURAL AND KINETIC CONSIDERATIONS	67
5. FUTURE WORK	70
6. CONCLUSIONS	71
7. ACKNOWLEDGMENTS	72
8. REFERENCES	72
APPENDIX	75

LIST OF TABLES

		<u>Page</u>
1.	Nominal and actual composition of Type 310S stainless steel	4
2.	Electropolishing conditions for Type 310S specimen blanks	6
3.	Exposure conditions for 310S specimens	13
4.	Deformation of ell-shaped specimens in air at 800 and 900°C	18
5.	X-ray diffraction data for specimen AR7; alloy 310S before exposure in air at 900°C	20
6.	Qualitative EDS analyses for specimen E1R3 after 120-h exposure in air at 900°C (summary of relative elemental abundance)	22
7.	Room-temperature X-ray diffraction data for specimen AR7 after 5-h exposure in air at 900°C	24
8.	Qualitative EDS analyses for specimen AR1 after 24-h exposure in air at 900°C (summary of relative elemental abundance)	29
9.	X-ray diffraction data for specimen AR1 after 24-h exposure in air at 900°C	31
10.	Qualitative EDS analyses for specimen AR4 after 216-h exposure in air at 900°C (summary of relative elemental abundance)	35
11.	Qualitative EDS analyses for specimen AR4 after 216-h exposure in air at 900°C (summary of relative elemental abundance)	36
12.	X-ray diffraction data for specimen AR6 after 384-h exposure in air at 900°C (File CT357C)	37
13.	Deformation of ell-shaped specimens in the "lean" sulfidizing atmosphere at 900°C	40
14.	Qualitative EDS analyses for specimens E1R4, E1R5, and AR8 after 24-h exposure in the "lean" sulfidizing atmosphere (summary of relative elemental abundance)	44
15.	Qualitative EDS analyses for specimen AR8 after 24-h exposure in the "lean" sulfidizing atmosphere at 1000°C (summary of relative elemental abundance)	45

	<u>Page</u>
16. X-ray diffraction data for specimen E1R5 after 24-h exposure in "lean" sulfidizing atmosphere at 900° C	46
17. Qualitative EDS analyses for specimen E1R6 after 216-h exposure in the "lean" sulfidizing atmosphere at 900° C (summary of relative abundance)	49
18. Qualitative EDS analyses for specimen E1R8 after 216-h exposure in the "rich" sulfidizing atmosphere at 900° C (summary of relative elemental abundance)	54
19. Qualitative EDS analyses for specimen E1R8 after 216-h exposure in the "rich" sulfidizing atmosphere at 900° C (summary of relative abundance)	56
20. Qualitative EDS analyses for specimen AR11 after 2-h exposure in the "rich" sulfidizing atmosphere at 900° C (summary of relative elemental abundance)	58
21. X-ray diffraction data for specimen AR11 after 2-h exposure in "lean" sulfidizing atmosphere at 900° C	59
22. Melting temperatures of selected metal sulfides and eutectic temperatures ¹³	64
23. Relative sulfur abundance in special CaSO ₄ lot	70

LIST OF FIGURES

	<u>Page</u>
1. Typical "flat" and "ell"-shaped 310S specimens prior to exposure	5
2. Mandrel used to bend "ell"-shaped specimens in a consistent manner	7
3. Typical quartz vessel used in the air oxidation of flat specimens	8
4. Furnace fixture used in the air oxidation of flat specimens	9
5. Quartz capsule used in the exposure of specimens to sulfidizing gases (shown prior to the loading and re-fusing operations)	10
6. Quartz capsule used in the exposure of specimens to sulfidizing gases (shown after the final sealing operation)	12
7. Photomicrograph of a transverse section of specimen E1R3 after 120-h exposure in air at 900° C (glyceric acid etch)	21
8. Electron micrograph showing the transverse scale structure of specimen E1R3 after 120-h exposure in air at 900° C	21
9. Changes in the interplanar spacing of scale compounds on specimen AR7 during its early exposure in air at 900° C	27
10. Square of specific mass gain as a function of time for specimens exposed in air at 900° C	28
11. Electron micrographs showing the scale structure of specimen AF1 after 24-h exposure in air at 900° C	29
12. Photomicrograph of a transverse section of etched specimen AR4 after 216-h exposure in air at 900° C	33
13. Electron micrographs showing the scale structure of specimens AR4 and AR5 after exposure in air at 900° C	34
14. Square of specific mass gain as a function of time for specimens exposed in the "lean" sulfidizing atmosphere at 900° C	40

	<u>Page</u>
15. Electron micrographs showing the scale structure of specimens E1R4 and AR8 after exposure in the "lean" sulfidizing atmosphere	42
16. Electron micrographs showing the scale structure of specimens E1R5 and E1R7 after exposures in the "lean" sulfidizing atmosphere at 900°C	43
17. Micrographs of the transverse scale structure of specimen E1R6 after 216-h exposure in the "lean" sulfidizing atmosphere at 900°C	48
18. Square of specific mass gain as a function of time for specimens exposed in the "rich" sulfidizing atmosphere at 900°C	51
19. Photomicrograph of a transverse section of specimen AR11 after 2-h exposure at 900°C in the "rich" sulfidizing atmosphere (Glyceregia etch)	52
20. Photomicrograph of as-polished transverse section of specimen AR11 after 2-h exposure at 900°C in the "rich" sulfidizing atmosphere	52
21. Photomicrograph of etched transverse section of specimen E1R8 after 24-h exposure at 900°C in the "rich" sulfidizing atmosphere	54
22. Electron micrographs of the scale structure of specimen E1R8 after 24-h exposure in the "rich" sulfidizing atmosphere at 900°C	55
23. Electron micrographs of the scale structure of specimen AR11 after 2-h exposure in the "rich" sulfidizing atmosphere at 900°C	57
24. Thermochemical diagram at 900°C for the constituents of 310S illustrating their critical oxygen and sulfur potentials, the atmospheres used in the research, and the gas potentials associated with the coal gasification regime	63

THE OXIDATION OF TYPE 310S STAINLESS STEEL IN MIXED GASES AT ELEVATED TEMPERATURES*

James S. Wolf[†], O. Burl Cavin, and J. H. DeVan

ABSTRACT

Sheet specimens of Type 310S stainless steel were exposed to air as well as to "lean" and "rich" sulfidizing atmospheres at temperatures near 900°C to determine the relationships that exist between the scale structure, the rate of reaction, and the stresses generated during exposure. One goal of this experimental research program was to examine how these factors might be related to the breakdown of protective scales in sulfidizing atmospheres.

It was found that the scales formed in air and the "lean" atmosphere are protective and non-spalling while those formed in the "rich" atmosphere spall, initially react at rates 1,000 times greater than their counterparts in less aggressive atmospheres, and later exhibit a "breakaway"-type rapid reaction. Only those scales formed in air provide the cooperative, tractive interfacial forces required to produce uniform dilatation and deformation of the substrate. However, evidence exists for at least localized stresses in all of the scales examined.

The two-layer scales formed both in air and in the "lean" atmosphere exhibit an inner sesquioxide and an outer spinel layer; however, the crystalline nature and surface topography of the scales formed in these two atmospheres is grossly different which may, in part, account for the observed differences in macroscopic specimen deformation. Metallic particles found embedded in the scale layers of specimens exposed to the "lean" sulfidizing atmosphere may be indicative of a stage in scale evolution, which is a precursor to the breakdown process of the protective scale. In contrast, scales formed in the "rich" atmosphere are very complex, having a minimum of six scale layers as well as subscale product formation. Liquid sulfides are present at 900°C and may permeate the inner suite of layers via a vein-like network.

It was concluded that the transport of sulfur through scale layers is an issue that has a strong bearing upon the micro-structure, the state of stress, the barrier quality, and ultimately the potential for breakdown of scales formed in sulfidizing atmospheres. It is, therefore, suggested that the control of oxide grain size may prove to be a fruitful approach in the future development of sulfidation-resistant alloys, and a tentative experimental plan to probe the basis of that possibility is outlined.

*Research sponsored by the U.S. Department of Energy, Assistant Secretary for Conservation and Renewable Energy, Office of Transportation Technologies, as part of the High Temperature Materials Laboratory User Program, and Office of Fossil Energy, Advanced Research and Technology Development (AR&TD) Materials Program, under contract DE-AC05-84OR21400 with Martin Marietta Energy Systems, Inc.

[†]Professor of Metallurgy, Department of Mechanical Engineering, Clemson University, Clemson, S.C.

1. INTRODUCTION

It has been pointed out that the economy of our country is closely tied to its energy reserves, foreign and domestic, and to the technical methodology that we employ to drive the machinery of our economy. Recently, it has been strongly suggested that we keep our energy-production options open by using our tremendous coal reserve in preference to oil and gas.¹ One major problem in coal utilization is the selection of materials of construction for long-term applications. A common requirement is the need for components to operate in the presence of both oxygen- and sulfur-bearing gases at elevated temperatures where metallic materials are subject to deterioration. An often-cited mode of deterioration is the loss of an initially protective quality of the scales formed upon metallic surfaces under such conditions—a phenomenon termed "breakaway" corrosion. This phenomenon is especially prevalent for those alloys that depend upon the establishment of chromium-rich scales for their protection at high temperatures. Many engineering and some scientific studies have been made; however, a recent review of the breakaway phenomenon indicates that we still know little about its origin, except that it may possibly be associated with stress development in scale layers.²

It is well known that if any metal or alloy is to display outstanding corrosion resistance in a particular environment, then that material must either be noble or it must develop a stable barrier film in that environment. The purpose of the barrier film or scale is, of course, to isolate and insulate the metallic component from the aggressive environment. Some of the methods for producing barrier layers on alloys have recently been summarized and, among those methods, the development of alloys with self-building alumina, chromia, or silica barrier layers is of particular interest.³ Thus, it appears that, in order to design barriers of superior quality, we must comprehend the details of their formation and structure so that we can control the transport of material through them. An obvious point at which to start this process of understanding is to examine the naturally formed barrier layers as they are produced upon commercial alloys and in environments of interest to those engaged in the development of economic energy systems.

The purpose of this investigation was to examine the structure of naturally formed scales on one alloy steel and to monitor its reaction kinetics with special reference to the breakaway phenomenon. One thesis of this work was that breakaway may be caused by the natural generation and relaxation of stresses in the scale when alloys are subjected to mixed oxidants at elevated temperature. Type 310S stainless steel was selected as the test material for this study on the basis that it is: (1) representative of potential alloys for the coal gasification environment,

(2) readily fabricable and readily available, and (3) it was initially compounded for high-temperature heat and cyclic oxidation resistance.⁴ Thus, future alloy development programs for coal utilization may well adapt compositions of this type as a starting point.

The behavior of Type 310S stainless steel was investigated at temperatures near 900°C, both in air and in simplified sulfidizing atmospheres that bracket the extremes of those atmospheres associated with the coal gasification regime. The initial focus of this program involved the determination of the rates of chemical reaction, the deformation suffered by the steel due to its high-temperature exposure, and the chemical nature of the reaction products that formed, as well as their crystallography and geometric disposition, upon the metallic substrate. From such knowledge, it was hoped to gain some understanding of the problem of scale breakdown.

2. PROCEDURE

In this section of the report are listed the details of this experimental program including the material investigated, its fabrication into specimens, the exposure of those specimens to oxidizing/sulfidizing conditions, and the methods of analysis employed in the examination of specimens. Four general types of specimen exposures were utilized: (1) exploratory tests, (2) baseline oxidation tests in air, (3) exposures in "lean" sulfidizing atmospheres, and (4) exposures in "rich" sulfidizing atmospheres.

2.1 MATERIALS

The single metallic specimen material selected for this study was Type 310S stainless steel. Among the relatively formable austenitic stainless steels, this grade is known for its resistance to high-temperature oxidizing environments, which results primarily from its high chromium and nickel content.⁵ Both the nominal and actual compositions of this alloy are detailed in Table 1. It is noted that the actual composition of this alloy is within the nominal analysis with one exception, the presence of the reactive element titanium. The presence of titanium was verified by independent means (energy-dispersive spectroscopy analyses discussed later).

Tests conducted in air required no special oxidizing reagents, while those conducted in the "lean" simulated sulfidizing atmosphere utilized a technical grade of calcium sulfate in order to generate the reactive gaseous atmosphere. The CaSO_4 used here was a 10 to 20 mesh size fraction

Table 1. Nominal and actual composition of Type 310S stainless steel

Element	Weight percentage	
	Nominal ⁵	Test alloy ⁶
Chromium	24 to 26	25.0
Nickel	19 to 22	20.0
Manganese	2.0 max	1.8
Silicon	1.50 max	0.47
Carbon	0.08 max	0.062
Titanium	0.00	0.05
Phosphorous	0.045 max	0.044
Sulfur	0.03 max	0.007
Iron	Balance	Balance

of the commercial product known as Drierite. For tests conducted in the "rich" sulfidizing atmosphere, a mixture of CaSO_4 and triple-distilled elemental sulfur was used, the mixture being stoichiometric with respect to the production of SO_2 by complete reaction. A discussion of the reactive atmospheres produced by these techniques is presented in the Appendix.

2.2 SPECIMEN DESIGN

Two different specimen geometries were used in this program: a "flat" specimen (designated as the AR series) and an "ell"-shaped specimen (designated as the E1R series). Both geometries are illustrated in Fig. 1. The flat specimens had a single hole at one end for suspension purposes, while the "ell" specimens had a similar hole for suspension at one end and, additionally, two holes at the opposite end for the purpose of determining dilatation. These two types of specimens were intended for two different purposes. The primary use of the flat specimens was to secure kinetic and microstructural data related to the oxidation and sulfidation of the 310S material. The "ell"-shaped specimens were designed to secure strain-related as well as kinetic and microstructural data.

The "ell"-type specimens were designed to sense strain in two ways. First, the convex and concave surfaces of an "ell-shaped" specimen are of different length; thus, reactions dependent upon the extent of interfacial area may generate stresses of sufficient magnitude to cause "ell"

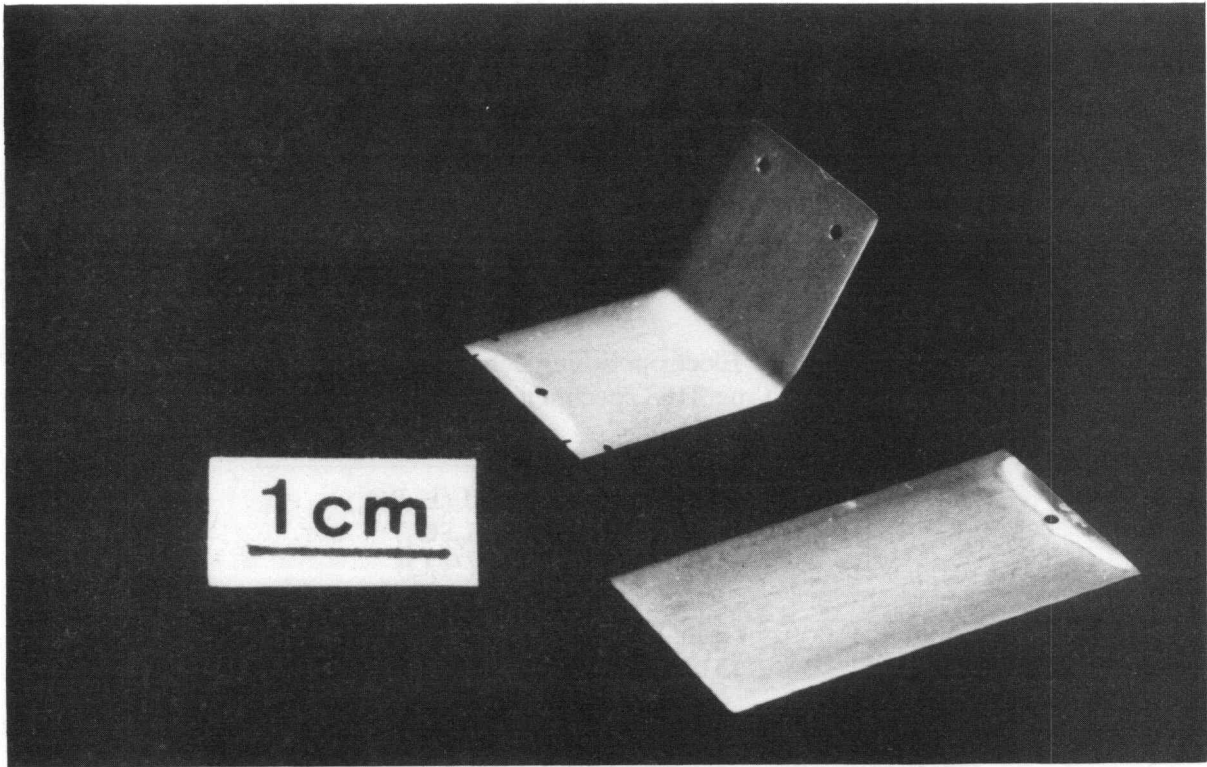


Fig. 1. Typical "flat and "ell"-shaped 310S specimens prior to exposure.

closure during exposure.⁷ Second, the two fiducial holes located near the end "ells" may be used to determine the planar dilatation of the thin-sheet specimens if one monitors the separation of their centers as a result of exposure.⁷ The primary assumptions for this case are: (1) that the out-of-plane warp is negligible and (2) that the hole edges are symmetrically altered as a result of exposure.

2.3 SPECIMEN PREPARATION

All specimens for this program were fabricated from the same lot of material, a portion of 310S plate stock having the dimensions $12 \times 1.5 \times 0.063$ in.* This material was cold rolled

*Although the policy of the Oak Ridge National Laboratory is to report its work in SI units, primarily customary units are used in this report. The engineering industry and the X-ray diffraction community presently use the customary units. The usage of the SI units would limit the usefulness of this report to the primary readership.

to a thickness of 0.013 in., hydrogen annealed at 900°C for 15 min, and then finish rolled to 0.010 gage. Specimen blanks, nominally 1 by 0.5 in., were sheared from this stock with the 1-in. dimension being parallel to the rolling direction.

Subsequent to drilling the 1/32-in.-diam suspension and fiducial holes, the flat faces of the specimens were manually ground on 600-grit SiC metallographic paper using double-sided tape to fix them to a backing block. Each blank was then electropolished under the conditions shown in Table 2.

Table 2. Electropolishing conditions for Type 310S specimen blanks

Electrolyte:	45% phosphoric acid (H_3PO_4) 40% sulfuric acid (H_2SO_4) 15% distilled water (H_2O)
Temperature:	Room temperature (25°C nominal)
Cathode:	3-in.-diam perforated stainless steel
Anode:	310S specimen blank
Potential:	24 V, closed circuit
Current:	27 A (nominal); $CD = 27 A/in.^2$
Duration:	15 (nominal)

After electropolishing, the specimens were rinsed in distilled water to remove the residual electrolyte, and the lengths of those specimens to be formed into "ells" were measured. The electropolishing operation was found to remove approximately 0.0002 in. of material from each face of the specimen. In order to produce "ells" of a consistent shape, a mandrel with a cylindrical radius of 1/8 in. was fabricated for the purpose of bending the flat sheet; this device is illustrated in Fig. 2. The specimens were then placed in an alumina boat, in groups of seven or eight, and were provided a stress-relief anneal in flowing hydrogen for a period of 5 min at 900°C. As this process produced a very thin tarnish layer, the specimens were subsequently re-electropolished to a bright finish using the procedure outlined above.

At this point, the mass of each specimen was determined using a five-place Mettler Model AE 240 analytical balance. The major dimensions of the specimens were determined to the nearest 0.0001 in. using vernier calipers, and the diameters of all holes, including the center-to-center separations of the fiducial holes for the "ell" specimens, were determined to the same accuracy using a Nikon Measurescope Model II equipped with electronic readout. In addition,

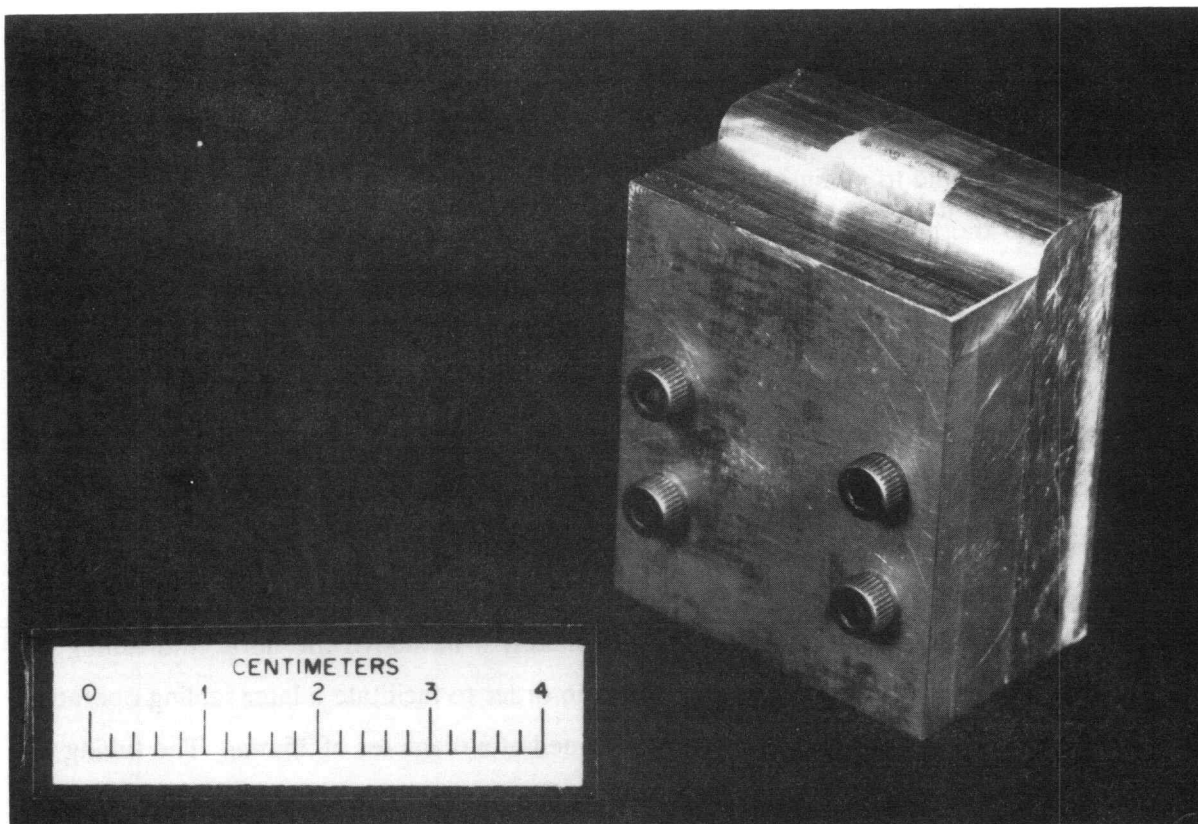


Fig. 2. Mandrel used to bend "ell"-shaped specimens in a consistent manner.

the bend angles for the annealed "ell" specimens were determined to the nearest 0.5° using a protractor method. The finished specimens were stored in capped, glass vials prior to their exposure.

2.4 EXPOSURE APPARATUS

Two different approaches were used in the conduct of these experiments, both of which involved the exposure of specimens in vertical muffle furnaces. In the first, specimens were exposed to air, while in the second, they were encapsulated in quartz also containing either CaSO_4 alone or admixed with elemental sulfur and exposed to the resulting gaseous dissociation products. For all tests, the upper surfaces of the furnaces were covered with a blanket of Fiberfrax insulation in order to both maintain constant temperature and to throttle the air flow through the furnace. In most instances, temperatures were controlled to within 1°C .

In preliminary exposures in air, "ell"-shaped specimens were hung in the hot zone of the furnace with Nichrome wires. Later exposures in air employed open quartz vessels within which flat specimens were suspended by platinum wires during oxidation (see Fig. 3). The purposes of these vessels were to retain any scale spall, which might occur at temperature or during subsequent cooling, and to minimize contamination during exposure. In order to maintain their alignment within the bore of the vertical furnace during oxidation, these vessels were, in turn, hung by Nichrome wires from the stainless steel furnace fixture illustrated in Fig. 4. This technique permitted the removal of individual specimens after a series of predetermined exposure times.

Those specimens to be exposed to sulfidizing atmospheres were mounted individually in specially designed quartz capsules prior to their exposure at elevated temperature. The capsules were fabricated from 25-mm OD quartz tubing as follows. A small quartz hook was installed approximately 4 in. from one end of the tubing, and the other end was subsequently closed to form the hemispherical capsule bottom. Approximately 4 in. above the hook, the tubing was constricted to a diameter of approximately 15 mm in order to facilitate a later sealing operation; the 12-in. section below the restriction was maintained at a diameter of 25 mm. The tubing was then cut radially with an abrasive saw to permit emplacement of the specimen. The resulting capsule configuration, prior to loading, is shown in Fig. 5.

YP5146

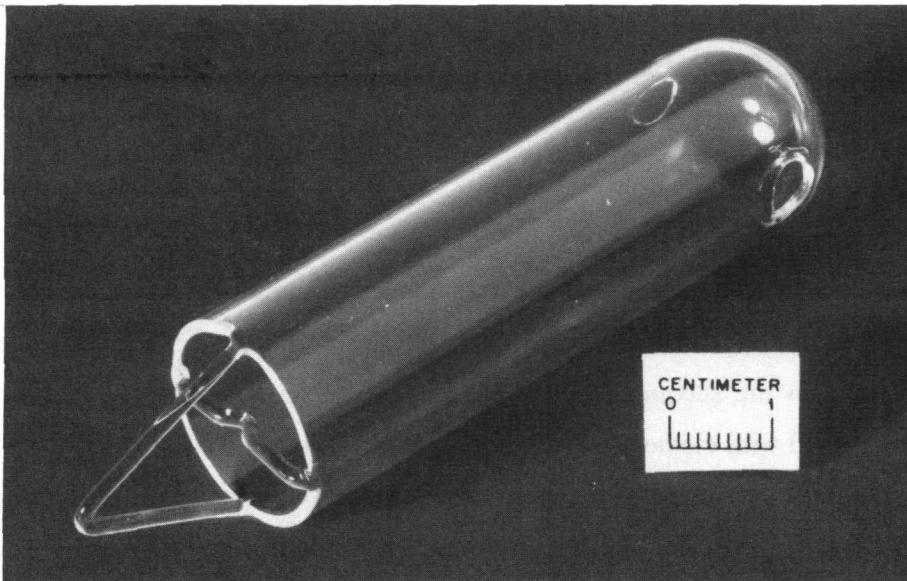


Fig. 3. Typical quartz vessel used in the air oxidation of flat specimens.

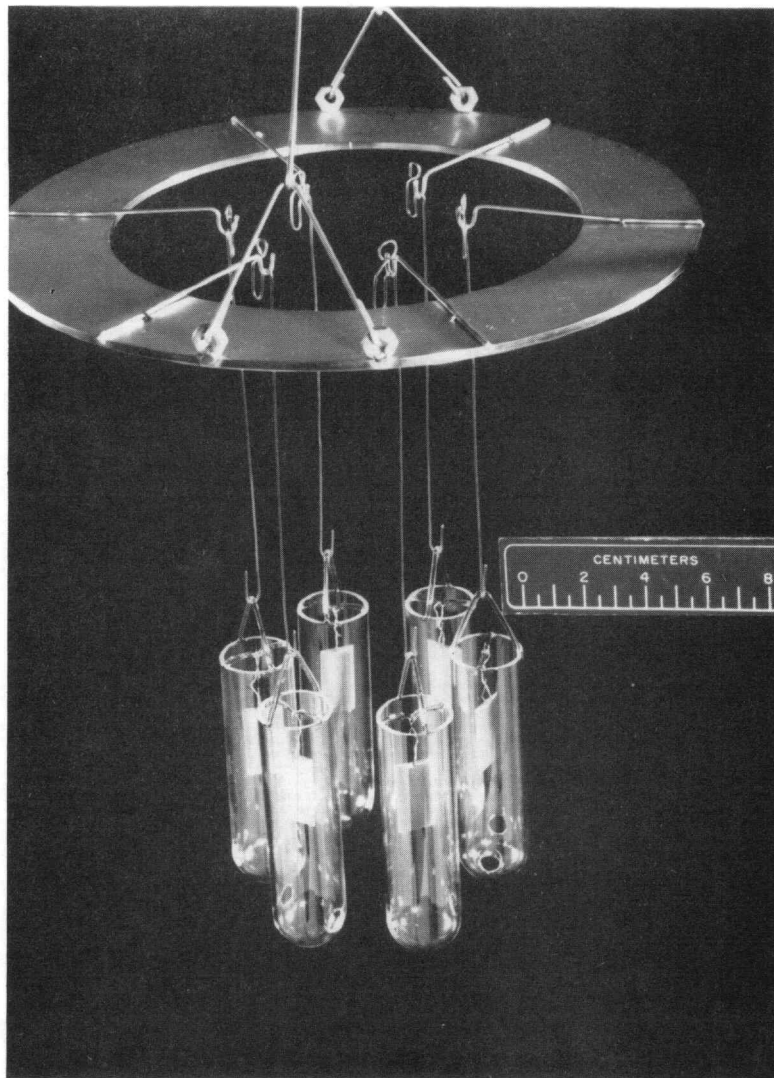


Fig. 4. Furnace fixture used in the air oxidation of flat specimens.

YP5182

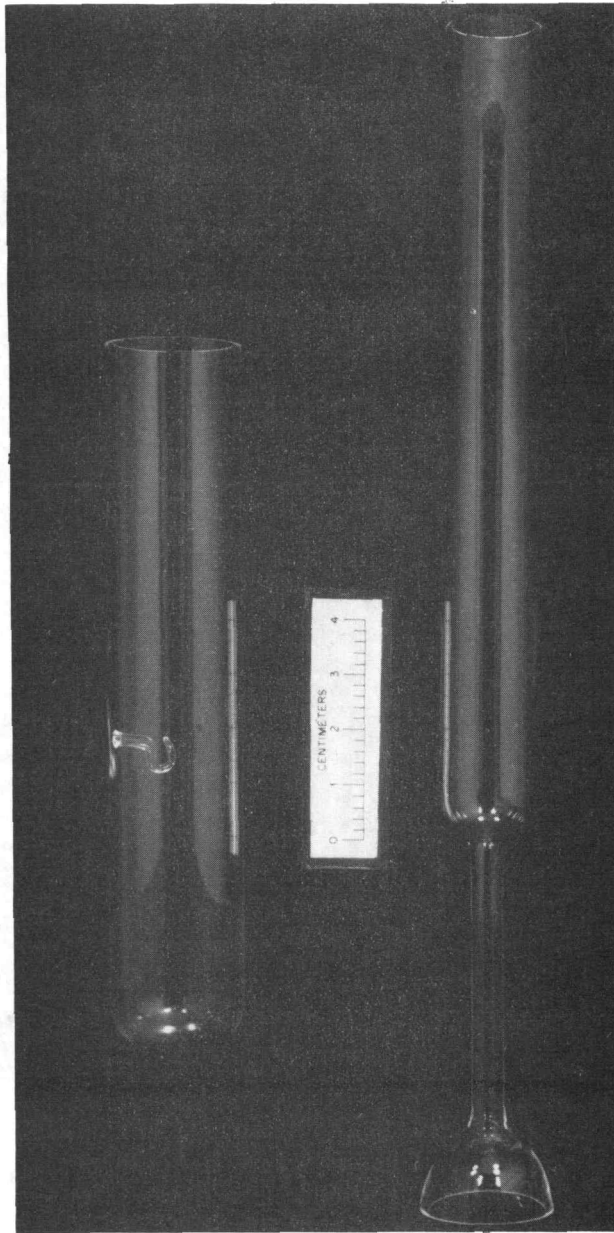


Fig. 5. Quartz capsule used in the exposure of specimens to sulfidizing gases (shown prior to the loading and re-fusing operations).

As indicated above, two types of sulfidizing atmosphere were investigated in this research. For tests run in the "lean" sulfidizing atmosphere, which is characterized by lower sulfur pressures, a small charge (nominally 1 gram) of CaSO_4 was wrapped in platinum foil and placed in the bottom of the capsule. For tests run in the "rich" sulfidizing atmosphere, the charge was comprised of approximately 8.5 parts of CaSO_4 and one part of elemental sulfur. The sulfur content of this charge was limited to a maximum of 10 mg in order to ensure that the pressure within the capsule would remain subatmospheric; i.e., nominally 0.36 atm at a temperature of 900°C for the 42 cm^3 capsule volume. This type of charge was similarly wrapped in platinum foil and placed in the bottom of the capsule.

Subsequent to the selection and emplacement of the gas-generating charge, the specimen was hung in the capsule from its quartz hook by means of a platinum wire and in a manner which ensured that it would touch neither the side of the capsule nor the charge packet. While maintaining the capsule in a vertical position, it was resealed along the line of the saw cut, taking care not to heat the specimen during the fusing operation. The capsule assembly was then evacuated to a pressure of 10^{-7} torr. For the cases involving "lean" atmosphere charges, the capsule was baked at a temperature of 200°C for a period of approximately 16 h while being evacuated for the purpose of removing any residual, adsorbed water vapor or other gases. For charges involving "rich" atmosphere generation, the baking step was omitted in order to avoid loss of sulfur from the charge. Subsequently, the capsule was sealed under vacuum to produce the finished assembly illustrated in Fig. 6. Such assemblies were heated in vertical furnaces, thus exposing the enclosed specimens to the sulfidizing gaseous dissociation products.

2.5 SPECIMEN EXPOSURES

The specimens used in this research were exposed either in air or suspended in sealed quartz capsules containing calcium sulfate. The latter ones were heated to produce the sulfidizing conditions. Tests were conducted at temperatures ranging from 800 to 1000°C and for times between 2 and 384 h (16 d). A summary of the exposure conditions is presented in Table 3.

Two preliminary tests were run in air at 800°C using specimens that had been surface finished using 600-grit SiC without the benefit of electropolishing. These specimens, having 90° manual bends and lacking stress-relief anneals, were exposed for 1 and 4 d primarily to determine qualitatively the magnitude of the stresses developed during oxidation.

YP5351

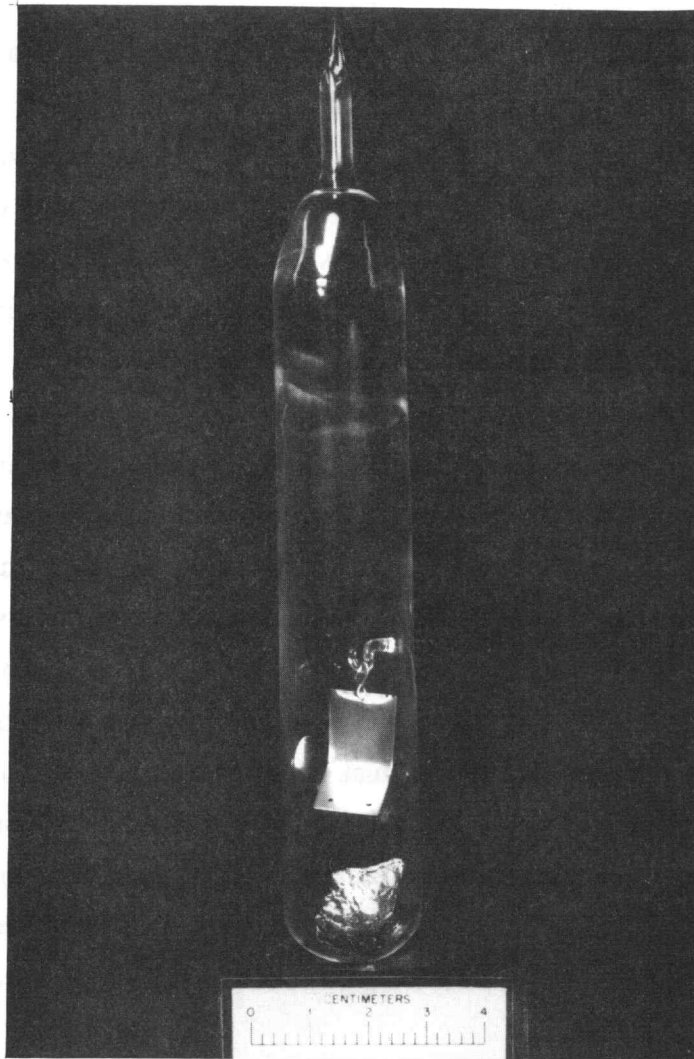


Fig. 6. Quartz capsule used in the exposure of specimens to sulfidizing gases (shown after the final sealing operation).

Table 3. Exposure conditions for 310S specimens

Specimen number	Specimen geometry	Temperature (°C)	Time (h)	Atmosphere type/source
Preliminary tests				
E1R1	E11	800	24	Air
E1R2	E11	800	96	Air
E1R10	E11	900	24	Air
E1R3	E11	900	120	Air
AR7	Flat	900	5	Air*
Baseline air oxidation tests				
AR1	Flat	900	24	Air
AR2	Flat	900	24	Air
AR3	Flat	900	96	Air
AR4	Flat	900	216	Air
AR5	Flat	900	384	Air
AR6	Flat	900	384	Air
Lean sulfidizing atmospheres				
E1R4	E11	800	24	CaSO ₄
E1R5	E11	900	24	CaSO ₄
E1R6	E11	900	216	CaSO ₄
E1R7	E11	900	384	CaSO ₄
AR8	Flat	1000	24	CaSO ₄
Rich sulfidizing atmospheres				
AR11	Flat	900	2	CaSO ₄ +S
E1R9	E11	900	4	CaSO ₄ +S
AR10	Flat	900	8	CaSO ₄ +S
AR9	Flat	900	24	CaSO ₄ +S
E1R8	E11	900	24	CaSO ₄ +S

*A special test dedicated to hot X-ray diffraction studies.

For the same primary purpose and to determine the influence of temperature upon the results, tests of ell-shaped specimens were run in air at 900°C for 1 and 5 d using specimens that had been electropolished; however, the latter did not receive the standard stress-relief anneal.

Six tests were run in air using flat specimens with surfaces prepared as outlined in Sect. 2.3 in order to secure "baseline" data for the oxidation of 310S in air. These tests were initiated simultaneously, using the furnace fixture shown in Fig. 4. The specimen assemblies were removed from the 900°C hot zone of the furnace at the following intervals: 1 d (2 each), 4 d, 9 d, and 16 d (2 each). These intervals were selected on the basis that oxidation might follow a parabolic (or slower) rate law.

Five tests were run in the "lean" sulfidizing atmosphere generated by the dissociation of calcium sulfate using quartz-encapsulated specimens and following the procedures outlined in Sects. 2.3 and 2.4. Two 24-h exploratory tests were conducted at temperatures of 800 and 1000°C, and the balance of the specimens were exposed at 900°C. The exposure intervals were selected to coincide, as practicable, with those for the "baseline" air tests.

Finally, five tests in quartz capsules were run at 900°C in the "rich" sulfidizing atmosphere generated by the dissociation of calcium sulfate - sulfur mixtures following the procedures outlined in Sects. 2.3 and 2.4. These tests were also run individually in vertical furnaces. Because of the relatively rapid reaction associated with the "rich" sulfidizing atmosphere, the test times ranged from 2 to a maximum of 24 h.

2.6 ANALYTICAL METHODS

The methods used to analyze exposed specimens included the following: (1) gravimetric analysis to determine the specific mass gain and from which to infer gross kinetic behavior; (2) metallographic analysis to determine especially the transverse structure of the scale; (3) scanning electron microscopy (SEM) and associated energy dispersive X-ray spectroscopy (EDS) to determine especially the surface structure of scales and their proximal chemistries; (4) low-energy, high-resolution SEM to provide more refined data for aspects 2 and 3 above; and (5) X-ray diffraction both at room and elevated temperatures to gain knowledge of details regarding the crystalline products within scales. Each of these methods is discussed below in the order presented here.

2.6.1 Mass and Dimensional Changes

Subsequent to removal from the furnace and natural cooling, each specimen was reweighed (with its spalled scale, if any) in order to determine the mass gain due to exposure. The mass increments were divided by the respective projected areas of the specimens to obtain the specific mass gains in units of mg cm^{-2} . Similarly, the critical dimensions of each specimen were determined after exposure. The changes in specimen shape, which were noted, thus represent the sum of those changes due to heating, high-temperature reaction, and cooling. A portion of the analyses below is based upon these mass and dimensional changes.

2.6.2 Metallography

Selected, exposed specimens were mounted "on edge" using a metallographic epoxy resin to which Coors pelletized alumina had been added for the purpose of edge retention. Immediately after pouring, the specimen mounts were degassed using a roughing vacuum in order to ensure the removal of residual air and to promote the adhesion of the epoxy to the specimen. Subsequent to hardening at room temperature, the mounted specimens were manually ground on silicon carbide metallographic papers to a 600-grit finish. Polishing operations were conducted using vibratory polishers in the following sequence: Pellon cloth with Linde-A abrasive, then nylon cloth with 1- μm diamond abrasive and, finally, nylon cloth with 1/2- μm diamond abrasive. This procedure produced well-polished specimens with a minimum of objectionable edge rounding.

In order to reveal the grain structure of the scale upon the alloy, the polished specimens were immersion etched for a period of 45 s. The etchant was comprised of one part saturated potassium ferricyanide solution and one part 50% sodium hydroxide stock solution and was utilized near 100°C. Subsequent to etching, each specimen was soaked at room temperature for 2 h in a cleansing solution comprised of one part ammonium hydroxide solution and four parts ethyl alcohol. Specimens so prepared were examined by optical microscopy, normal SEM, and high-resolution SEM techniques.

2.6.3 SEM and EDS

Two distinctly different presentations of the scale layers were analyzed using SEM techniques: (1) the topography of the gas-scale interface as viewed normal to the surface of unmounted specimens and (2) the transverse section of scales using mounted and etched specimens as developed metallographically.

In the first method, whole or partial specimens were mounted upon SEM stubs with silver-loaded paint and were carbon shadowed prior to insertion into the stage of the JEOL Model JSM-35CF scanning microscope. Both typical and special surface topographies were photographed, and, additionally, selected areas of the specimen surfaces were qualitatively analyzed for their chemical constitution using an integral Tracor-Northern Model TN 5500 X-ray Analyzer. Usual practice involved using a beam potential of 15 kV for photography and one of 25 kV potential for EDS. In the second method, etched specimens in epoxy metallographic mounts were striped with conductive, silver-loaded paint and were carbon shadowed prior to insertion into the stage of the JEOL SEM. Transverse sections of the scale and the alloy adjacent to it were photographed, and, additionally, some specimens were qualitatively analyzed for their chemical constitution as before. Selected specimens of this type, which exhibited very fine detail in the scale structure, were further examined using a Hitachi Model S-800 SEM. This instrument, capable of higher resolution than the JEOL Model JSM-35CF, was typically operated using a beam potential of 5 kV and was utilized only for photographic purposes.

It is noted that, in the analyses of EDS data, the instrumental interferences between chromium, manganese, and iron were deconvoluted arithmetically from the detector output. This was done by presuming that the integrated intensity of the K- α signal for each of these elements was 7.5 times that of their K- β peak. Thus, a qualitative analysis could be obtained by developing intensity ratios for the K- α excitations.

2.6.4 X-ray Diffraction

The crystal structures of the scales formed upon the surfaces of selected 310S specimens or of their spalled reaction products (and to some extent that of the substrate) were determined at both room and elevated temperatures by automated X-ray diffraction techniques. In all cases, X rays were generated using a tube with a copper target that was operated at 45 kV and 40 mA. Thus, a semiquantitative comparison of intensities from different diffraction patterns is possible provided the areas of the specimens exposed to the X-ray beam were comparable (as was the usual case).

In order, first, to determine the positions of significant diffraction maxima, room-temperature tests were conducted using a Scintag Model "PAD V" diffractometer. This instrument was operated in the $\theta/2\theta$ mode, and the diffracted radiation was detected with a liquid-nitrogen-cooled, solid-state, germanium crystal detector whose output was fed into a single-channel analyzer and stored for subsequent analysis. The resolution of this system is sufficient

to discriminate against all unwanted radiation except the desired $k\text{-}\alpha$ wave length. This output was analyzed using a Data General Model MV-2000 computer that could access a master file containing the JCPDS* diffraction standards. Through its capabilities of pattern searching and matching, second derivative peak searching and detection, data smoothing and profile matching, this system was capable of narrowing the field of potential crystal structures representing the observed pattern.

Because many of the scales evidenced both line broadening and specular reflections (the latter leading to intensity "spikes"), portions of many diffraction patterns were deconvoluted via an interactive computer program that permitted the input of operator judgement. A final judgement process, regarding the line assignment for each pattern, was made by one of the authors using the JCPDS diffraction standards in printed format, a process that also involved the calculation of lattice parameters for all cubic systems in order to ensure proper assignment of diffraction maxima.

Having determined the diffraction patterns of interest at room temperature, one specimen (AR7) was examined while undergoing oxidation in air at 900°C. This was accomplished using the Scintag Model "PAD X" diffractometer, which was outfitted with an Edmund Buehler Model HDK-2 hot stage. In this instrument, the specimen remains stationary in the horizontal position while the source and detector maintain a θ/θ relationship. This experiment was conducted by repeatedly scanning the same angular range (20 to 45°, 2 θ) in an attempt to monitor the evolution of crystallographic development and, in particular, to determine whether or not one crystalline phase exhibited evidence for strain generation. The X-ray generation, detection, and analysis details were otherwise similar to those described above for room-temperature investigations.

3. RESULTS

Results are presented in the order of the four types of specimen exposure that were utilized: (1) preliminary tests, (2) baseline oxidation tests in air, (3) exposures in "lean" sulfidizing atmospheres, and (4) exposures in "rich" sulfidizing atmospheres.

*Joint Committee on Powder Diffraction Standard.

3.1 PRELIMINARY TESTS

Four exploratory tests were run at 800 and 900°C using ell-shaped specimens primarily to determine: (1) semi-quantitatively, the kinetics of the reaction and (2) qualitatively, the magnitude of the stresses generated during the oxidation process. At both temperatures, the rates of oxidation were found to be essentially parabolic. The mass gains were, therefore, fit to the parabolic rate law: $W^2 = kt$ where (W , mgcm^{-2}) is the specific mass gain; (t , h) is the exposure time; and (k , $\text{mg}^2\text{cm}^{-4}\text{h}^{-1}$) is the parabolic rate constant. The rates of mass gain exhibited by the specimens exposed at 800°C were small, having an average value of $1.17 \times 10^{-3} \text{ mg}^2\text{cm}^{-4}\text{h}^{-1}$. The corresponding value of the parabolic rate constant at 900°C was found to be approximately $6.57 \times 10^{-3} \text{ mg}^2\text{cm}^{-4}\text{h}^{-1}$. No significant spalling was noted for specimens oxidized in air at either of these temperatures.

The deformations suffered by these four specimens as a result of their oxidation in air are summarized in Table 4.

Table 4. Deformation of ell-shaped specimens in air at 800 and 900°C

Specimen number	Exposure time (h)	Ells closure		Dilatation	
		Angle (deg)	Rate (deg/ \sqrt{h})	Linear (%)	Rate (1/ \sqrt{h})
Tests at 800°C - 90° ells - 600-grit finish					
E1R1	24	2	0.41	N/A	N/A
E1R2	96	4.5	0.46	N/A	N/A
Tests at 900°C - 120° ells - electropolished					
E1R10	24	26.3	5.37	1.73	0.353
E1R3	120	63.6	5.81	3.42	0.312

Specimens tested at 800°C had not been provided with either fiducial holes for determining dilatation or proper finishing treatments. Specimen E1R3 was nonstandard in that it had not received a stress-relief heat treatment. At both temperatures, a time-dependent,

angular closure occurred in spite of the fact that the gravitational forces should have produced an opening of the original bend angle. Further, for the 900°C tests, a dilatation of the gage length was noted that increased with exposure time. It was, thus, concluded that oxidation-induced stresses were causal to ell angle closure.

In view of the fact that the oxidation rate had been found to be parabolic, the rates of angle closure and linear dilatation were calculated on the basis that they, too, obeyed a parabolic relationship. As indicated in Table 4, these rates are essentially constant at a fixed temperature, indicating that the mechanical deformations are directly related to the oxidation process. It is interesting to note that, while the oxidation rate at 900°C was approximately 6 times that at 800°C, the rate of ell closure at 900°C was approximately 12 times that at 800°C. Thus, the mechanical deformation rates are sensitive to more than simply the rate of scale thickening and probably also reflect the decrease in creep strength of the alloy with rising temperature.

The type 310S starting material was initially characterized by X-ray diffraction. The results of the diffraction analysis, presented in Table 5, indicate that the intermetallic phase commonly known as "sigma" was present within the before-test microstructure of this alloy. No other crystalline phases were detected in the metallic specimens by X-ray methods.

Knowing that the 310S was essentially a two-phase alloy, the deformed specimen E1R3 was also examined rather intensively by metallographic, SEM, and EDS techniques in order to secure additional data regarding its structural nature. The general aspects of its structure are revealed in Fig. 7, which shows a transverse section of the entire specimen. A thin-scale layer, approximately 3 μm in thickness, is evident at the outer surface of the specimen. Underlying the scale is a zone of coarse austenite grains, approximately 50 μm in depth, which has been denuded of the sigma phase particles shown at the interior of the specimen. In that interior zone, the austenite crystals are smaller, their growth evidently having been retarded by the presence of the sigma phase particles, which are seen to reside primarily upon the grain-boundary network of the austenite.

Details of this scale's transverse structure were revealed using the etching procedure described in Sect. 2.6.2, followed by inspection using the Hitachi S-800 SEM. The electron micrograph of Fig. 8 shows that the scale is duplex, exhibiting two layers parallel to the alloy-oxide interface. The innermost layer is composed of fine columnar grains having a typical plan dimension of approximately 0.25 μm and a height of approximately 3 μm (aspect ratio of 12:1). Overlying this is a layer of unresolved structure having an average thickness of somewhat less than 1 μm . Portions of this scale layer may have been lost in processing the specimen. Of

Table 5. X-ray diffraction data for specimen AR7;
alloy 310S before exposure in air at 900°C

Diffraction data (austenitic matrix)			JCPDS card 33-397 (chromium iron nickel)		
Strong component					
2 θ	d (Å) ^a	I/I _o ^b	(hkl)	d (Å) ^a	I/I _o ^b
43.432	2.0818	65	(111)	2.075	100
50.641	1.8011	48	(200)	1.796	45
74.563	1.2717	100	(220)	1.269	26
90.594	1.0838	31	(311)	1.082	30
95.878	1.0375	4	(222)	1.037	12
118.096	0.8982	3	(400)	0.898	3
Diffraction data (sigma phase of alloy)			JCPDS card 5-708 (chromium iron)		
Medium component					
2 θ	d (Å) ^a	I/I _o ^c	(hkl)	d (Å) ^a	I/I _o ^c
39.266	2.2926	51	(002)	2.261	10
42.204	2.1395	39	(112)	2.128	100
Austenite interference-----			(330)	2.063	80
44.5327	2.0329	68	(202)	2.015	60
45.7669	1.9809	100	(212)	1.964	80
46.8344	1.9382	33	(411)	1.928	100
48.0626	1.8915	10	(331)	1.877	80
49.3219	1.8461	8	(222)	1.830	10
51.6246	1.7691	17	(312)	1.755	10
Not detected-----			(322)	1.664	1
Not detected-----			(431)	1.638	1
Not detected-----			(511)	1.611	1
67.225	1.3915	9	(432)	1.390	1
Not detected-----			(522)	1.327	1
Austenite interference-----			(532)	1.258	10
75.563	1.2573	9	(550)	1.244	10
76.7672	1.2406	10	(413)	1.236	40
77.1983	1.2347	5	(333)	1.224	20
77.6805	1.2282	18	(720) ^d	1.209	40
77.7701	1.2271	12	(720) ^d	1.209	40
Not detected-----			(423) (551)	1.199	10
Not detected-----			(622)	1.186	10
Not detected-----			(542) (641)	1.177	10
Not detected-----			(721)	1.169	10
Not detected-----			(513)	1.138	40
99.872	1.0065	19	(414)	1.004	20

^aa_o = 3.5944 Å; strong (110) texture.

^bI_o = 42383 cpm.

^cI_o = 5044 cpm.

^dDenotes a doublet not resolved in the JCPDS reference.

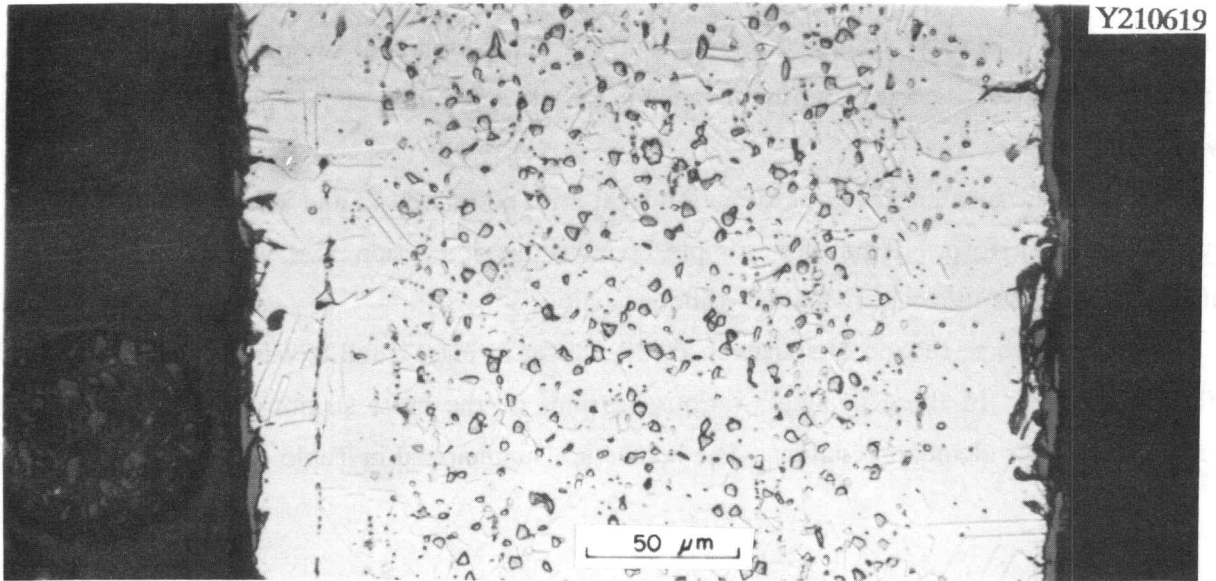


Fig. 7. Photomicrograph of a transverse section of specimen E1R3 after 120-h exposure in air at 900° C (glyceregia etch).

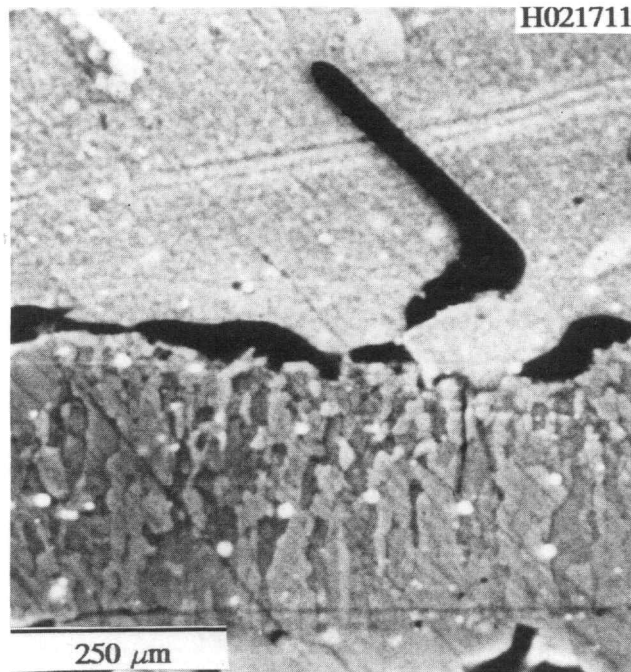


Fig. 8. Electron micrograph showing the transverse scale structure of specimen E1R3 after 120-h exposure in air at 900° C.

additional interest in this figure are: (1) a crack near the interface between the scale layers, but just within the underlying columnar crystals, and (2) the existence of smooth voids both at the metal-oxide interface and, apparently, at the junction of the grain-boundary network of the alloy with that interface.

Obviously, such prolific void formation must both be related to and affect the mechanism by which the scale forms. It may, for example, be indicative of reaction rates, which decrease with time, and may also reflect very limited oxide plasticity.

The transverse section of specimen E1R3, shown in Figs. 7 and 8, was also examined by EDS techniques. In these analyses, various portions of the cross section were qualitatively analyzed for their elemental content. The results are summarized in Table 6.

Table 6. Qualitative EDS analyses for specimen E1R3 after 120-h exposure in air at 900° C (summary of relative elemental abundance)^a

Chemical element	Position in transverse section ^b			
	(A)	(B)	(C)	(D)
Iron	100	100	100	100
Chromium	76	60	47	48
Nickel	22	23	23	22
Manganese	3	0.2	0	0
Silicon	2	3	2	4

^aRelative elemental abundance is in terms of each element's K- α excitation divided by that for the strongest element (presented as percentages).

^bKey to positions:

- (A): Sigma phase particle near center of section.
- (B): Denuded zone distal from the alloy-oxide interface.
- (C): Denuded zone proximal to the alloy-oxide interface.
- (D): Voided alloy grain boundary in denuded zone.

Additionally, it was shown that chromium and manganese both exist at appreciable concentration levels in the scale; however, as this specimen was not properly cleaned prior to EDS analysis, the numerical values (biased by contamination) are not presented here. Taken as a whole, the EDS data show that chromium and manganese are depleted from the subsurface zone of the alloy to participate in scale building, while the nickel and silicon concentrations appear to be little affected by oxidation. (It will later be shown that silicon does, in fact, participate in the oxidation reaction.)

The last of the preliminary tests was directed toward the generation of information regarding the crystalline nature of the reaction products and their evolution. During this test, specimen AR7 was simultaneously subjected to oxidation in air at 900°C and to analyses by X-ray diffraction, described in Sect. 2.6.4. The diffraction data representing mean oxidation times of 0.25, 0.5, 1, 3, 3.75, and 5 h were stored temporarily while the specimen was cooled to room temperature, after which it was again x-rayed to determine which reaction products formed. The results of this analysis, detailed in Table 7, indicated that the primary reaction products were: (1) a spinel oxide similar in composition to MnFe_2O_4 , later shown to be an external scale layer, and (2) a sesquioxide similar in composition to Cr_2O_3 , later shown to be an inner scale layer. The intensities of the diffraction maxima associated with these products reinforce the relative positions of the scale layers just described.

Knowing the positions of the most intense reflections for the reaction products formed, the stored high-temperature diffraction data were then analyzed. For both compounds, it was found that the diffraction angle changed smoothly with time, as shown in Fig. 9. The lattice of the Cr_2O_3 -like compound decreased in dimension as time progressed and, further, consistently exhibited a very broad (0.4°) diffraction maxima for its (104) line. Such behavior, when coupled with the texture exhibited by the diffraction pattern as a whole, is indicative of a tractive force between the alloy and the inner scale layer, as occurs in epitaxial relations. Conversely, the lattice of the MnFe_2O_4 -like compound increased in dimension as time progressed and exhibited an early maximum in the breadth of the diffraction peak for its (311) line at about 1 h of exposure time. Such behavior, when coupled with the essentially textureless diffraction pattern as a whole, is indicative of a relatively slow change in lattice parameter, possibly due to selective elemental transport between the alloy and the outer scale layer. It is noted that some peak broadening does persist even in this outer scale layer, and such may be due to either compositional gradients or crystallographic strains within that layer or possibly both.

Table 7. Room-temperature X-ray diffraction data for specimen AR7 after 5-h exposure in air at 900°C

Diffraction data (austenitic matrix)			JCPDS card 33-397 (chromium iron nickel)		
Strong components					
2 θ	d (Å) ^a	I/I ₀ ^b	(hkl)	d (Å) ^a	I/I ₀ ^b
43.492	2.0791	58	(111)	2.075	100
50.714	1.7987	35	(200)	1.796	45
74.640	1.2706	100	(220)	1.269	26
90.674	1.0830	27	(311)	1.082	30
95.953	1.0369	3	(222)	1.037	12
118.303	0.8972	2	(400)	0.898	3
Diffraction data (Pt-Rh vapor deposit)			JCPDS card 4-802 (unalloyed platinum)		
2 θ	d (Å) ^c	I/I ₀ ^d	(hkl)	d (Å) ^c	I/I ₀ ^d
39.6161	2.2731	100	(111)	2.265	100
46.1056	1.9671	32	(200)	1.961	53
67.385	1.3886	15	(220)	1.387	31
81.207	1.1836	10	(311)	1.182	33
85.642	1.1333	3	(222)	1.132	12
Not detected	-----	-----	(400)	0.980	6
117.717	0.9000	3	(331)	0.900	22
Diffraction data (Pt-Rh strip heater)			JCPDS card 4-802 (unalloyed platinum)		
Medium components					
2 θ	d (Å) ^c	I/I ₀ ^e	(hkl)	d (Å) ^c	I/I ₀ ^e
39.4755	2.2809	100	(111)	2.265	100
45.8148	1.9788	45	(200)	1.961	53
67.119	1.3934	16	(220)	1.387	31
80.735	1.1893	11	(311)	1.182	33
85.642 ^f	1.1333	8	(222)	1.132	12

Table 7. (Continued)

Diffraction data (spinel oxide scale)			JCPDS card 10-319 (MnFe ₂ O ₄)		
2 θ	d (Å) ^g	I/I ₀ ^h	(hkl)	d (Å) ^g	I/I ₀ ^h
29.3496	3.0407	35	(220)	3.005	35
34.6008	2.5903	100	(311)	2.563	100
36.212	2.4786	16	(222)	2.450	12
42.229 ⁱ	2.1383	<22	(400)	2.124	25
Not detected-----			(422)	1.734	20
55.609	1.6514	20	(511)	1.635	35
61.124	1.5149	23	(440)	1.503	40
64.362 ^j	1.4463	<14	(531)	1.437	4
Not detected-----			(620)	1.344	4
72.212	1.3072	7	(533)	1.296	20
Not detected-----			(622)	1.281	15
77.689 ^k	1.2281	8	(444)	1.227	10
Platinum interference			(711)	1.190	12
Not detected-----			(642)	1.135	7
Not detected-----			(553)	1.106	30

Diffraction data (sesquioxide scale)			JCPDS card 35-112 (Cr ₁₃ Fe _{0.7} O ₃)		
Weak components					
2 θ	d (Å) ^g	I/I ₀ ^l	(hkl)	d (Å) ^g	I/I ₀ ^l
24.1472	3.6827	94	(012)	3.654	45
33.170	2.6986	100	(104)	2.676	100
35.706	2.5126	92	(110)	2.499	75
Platinum interference			(006)	2.270	4
40.929	2.2032	14	(113)	2.189	25
Austenite interference		16	(024)	1.827	35
49.421	1.8427	16	(024)	1.827	35
54.330	1.6872	54	(116)	1.680	65
Not detected-----			(122)	1.590	5
Not detected-----			(010)	1.585	6
Not detected-----			(214)	1.474	25
64.362 ^j	1.4463	<31	(300)	1.442	25
Not detected-----			(208)	1.338	1
72.212	1.3072	16	(10 10)	1.299	12
Not detected-----			(220)	1.249	6
77.689 ^k	1.2281	<18	(306)	1.218	3
Platinum interference			(128)	1.179	2
Not detected-----			(0 2 10)	1.152	4
85.642	1.1333	<32	(134)	1.132	7

Table 7. (Continued)

Diffraction data (sigma phase of alloy)			JCPDS card 5-708 (chromium iron)		
2 θ	d (Å) ^g	I/I ₀ ^m	(hkl)	d (Å) ^g	I/I ₀ ^m
Platinum interference			(002)	2.261	10
42.229 ^j	2.1383	100	(112)	2.128	100
Austenite interference			(330)	2.063	80
44.552	2.0321	92	(202)	2.015	60
Platinum interference			(212)	1.964	80
Not detected-----			(411)	1.928	100
48.233	1.8852	27	(331)	1.877	80
49.867	1.8272	63	(222)	1.830	10
Not detected-----			(312)	1.755	10
55.058	1.6666	94	(322)	1.664	1
Not detected-----			(431)	1.638	1
Not detected-----			(511)	1.611	1
Platinum interference			(432)	1.390	1
Not detected-----			(522)	1.327	1
Not detected-----			(532)	1.258	10
Not detected-----			(550)	1.244	10
76.808	1.2400	56	(413)	1.236	40
Not detected-----			(333)	1.224	20
77.689 ^k	1.2281	<38	(720)	1.209	40

$a_{a_0} = 3.5942 \text{ \AA}$; V.strong (110) texture.

$b_{I_0} = 31618 \text{ cpm}$.

$c_{a_0} = 3.926 \text{ \AA}$; some (111) texture.

$d_{I_0} = 11084 \text{ cpm}$.

$e_{I_0} = 3903 \text{ cpm}$.

f Line shared by Pt-RH heater and sesquioxide.

$g_{a_0} = 8.55 \text{ \AA}$.

$h_{I_0} = 2215 \text{ cpm}$. Spinel is highly strained, coarse grained.

i Line shared by spinel and sigma phase.

j Line shared by spinel and sesquioxide.

k Line shared by spinel, sesquioxide, and sigma phase.

$l_{I_0} = 918 \text{ cpm}$; some (110) texture).

$m_{I_0} = 477 \text{ cpm}$.

Note: Heater is not located on the focusing circle of the diffractometer; therefore, d-values are listed for information purposes only.

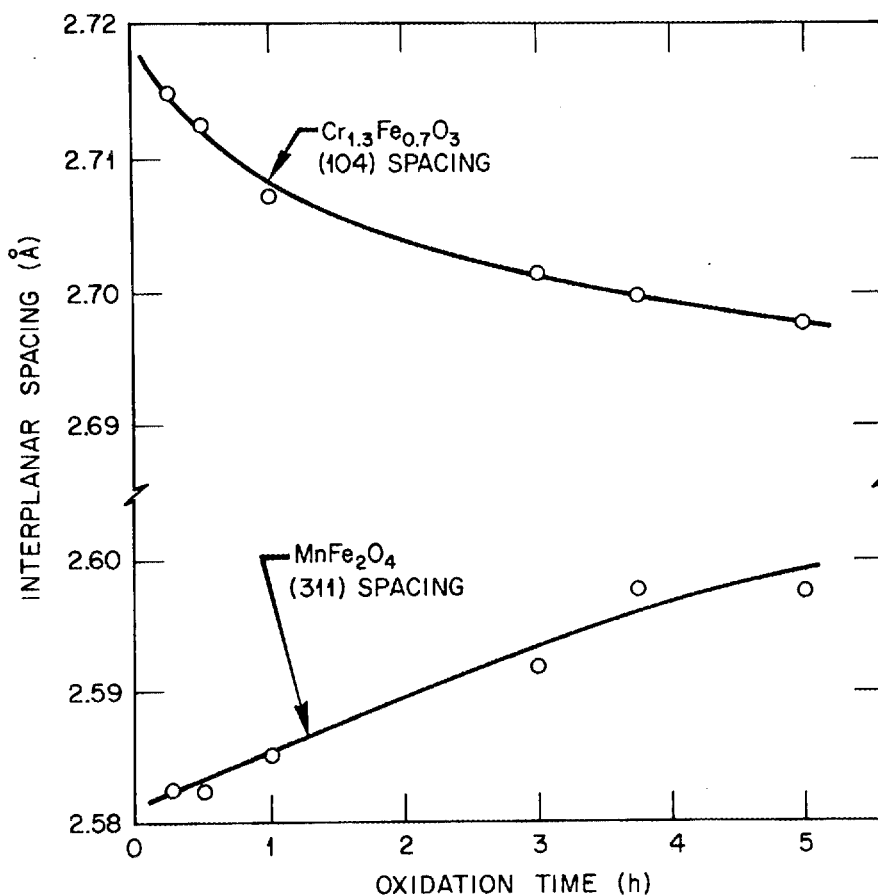


Fig. 9. Changes in the interplanar spacing of scale compounds on specimen AR7 during its early exposure in air at 900° C.

3.2 BASELINE OXIDATION IN AIR

The main purpose of this group of tests was to determine: (1) the kinetics of reaction of 310S in air and (2) structural information regarding the reaction products which formed. These data thus serve as a baseline against which to compare results obtained in sulfidizing atmospheres (discussed later). As flat specimens only were used in these 900° C exposures, no quantitative information regarding mechanical deformation was obtained.

The observed weight gains for the six specimens exposed in air for times up to 384 h (16 d) are shown in Fig. 10. The data indicate that, aside from an initial transient, the kinetics are essentially parabolic in character. The value of the parabolic rate constant associated with the linear portion of this graph has a value of $3.88 \times 10^{-3} \text{ mg}^2\text{cm}^{-4}\text{h}^{-1}$. This value is smaller than that found in the preliminary tests, wherein the existence of the transient was not recognized.

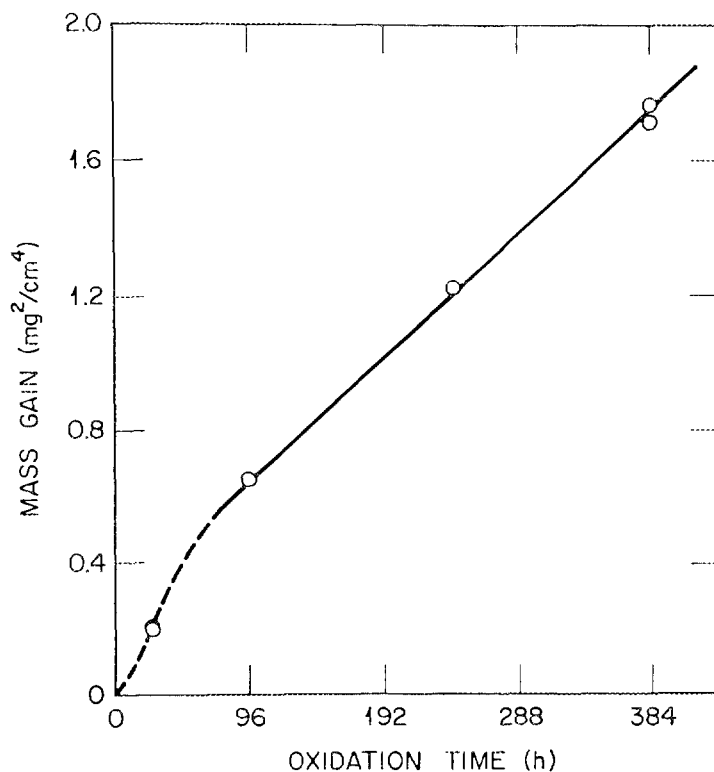


Fig. 10. Square of specific mass gain as a function of time for specimens exposed in air at 900° C.

Fortuitously, the transient portion of the weight gain curve can be approximated by a higher initial value of the parabolic rate constant. Thus, the argument presented in Sect. 3.1 regarding the relation between oxidation and deformation is retained.

The results of an EDS analysis for this same specimen after the 24-h exposure are summarized in Table 8. It appears from this analysis that the granular scale is rich in chromium and surprisingly rich in manganese, the other major alloy elements being essentially absent.

The structure of the air-formed scales developed on 310S after 24 h of exposure is shown in the electron micrographs of Fig. 11. The outermost portion of the scale is seen to be composed of faceted grains. Any special regularity in their shape is difficult to discern. The lower photograph, Fig. 11(b), illustrates an area of the specimen where spalling has occurred. A light filamentary network is seen to reside below the granular outer scale but above the alloy substrate. It appears that the network, at some prior time, may have been associated with the

Table 8. Qualitative EDS analyses for specimen AR1 after 24-h exposure air at 900°C summary of relative elemental abundance^a

Chemical element	Featured in normal section ^b		
	(A)	(B)	(C)
Iron	0	22	100
Chromium	100	11	40
Nickel	0	5	22
Manganese	39	1	0
Silicon	0	100	5.5

^aRelative elemental abundance is in terms of each element's K- α excitation divided by that for the strongest element (presented as percentages).

^bKey to positions:

- (A): External surface of the granular scale.
- (B): Filamentary network near the alloy-oxide interface.
- (C): Substrate grains near the alloy-oxide interface.

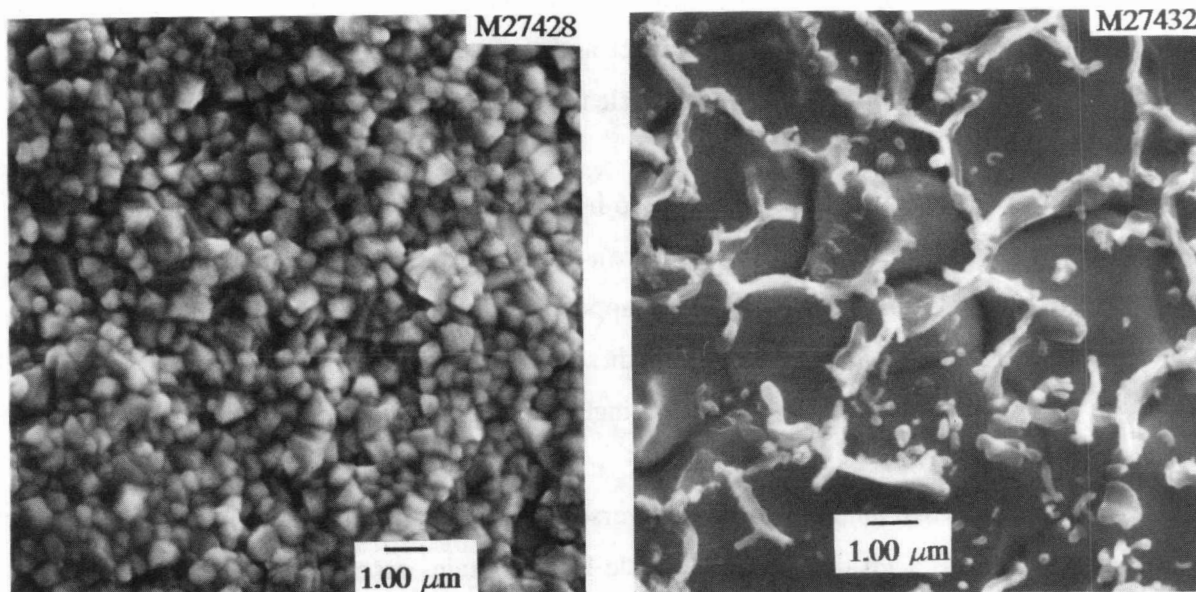


Fig. 11. Electron micrographs showing the scale structure of specimen AR1 after 24-h exposure in air at 900°C.

grain-boundary network of the alloy. The primary metallic element of the light-colored network of Fig. 11(b) is silicon; the compound may be essentially pure silica, as some "spillover" of signal from surrounding features is probable. Finally, at points of that same specimen (but between the filaments) is found what appears to be the austenite matrix depleted of manganese and perhaps somewhat enriched in silicon.

Inspection of specimen AR1 by X-ray diffraction indicated the presence of both a spinel and a sesquioxide as surface compounds, as shown in Table 9. However, no silicon-bearing compound could be identified in that diffraction pattern, indicating that the silicon, which had been found by EDS, may be in an amorphous form. While the spinel pattern was matched to the JCPDS card for MnFe_2O_4 , the EDS analysis indicates that it is more likely to be a compound of the general formulation $(\text{Mn,Cr})_3\text{O}_4$, the X-ray method being sensitive to crystal structure rather than chemical constitution. Similarly, the sesquioxide pattern was matched to the JCPDS card for $\text{Cr}_{1.3}\text{Fe}_{0.7}\text{O}_3$, while an EDS analysis to be presented shortly will indicate that it is more likely to be a distorted compound of the general formulation Cr_2O_3 .

The air-formed scales developed after 216-h (9-d) exposure at 900°C are more mature versions of those just discussed. Figure 12 illustrates an optical photomicrograph of a transverse section through specimen AR4, clearly showing a two-layered scale. The outer layer exhibits a relatively large and blocky grain size, while the inner layer is apparently of much finer structure. Details of this structure are more clearly evident in the electron micrograph of Fig. 13(a) where the inner layer appears to be relatively compact and composed of fine columns approximately $0.25\ \mu\text{m}$ in width. Beneath the scale, voids are clearly evident upon the grain-boundary network of the alloy.

While the structure shown in Fig. 13(a) (216-h exposure) is similar in kind to that developed at lesser times, as shown in Fig. 8 (120-h exposure), the detail of the external scale layer is clearer here, and the amount of interfacial voiding appears to be reduced. These differences are probably attributable to difficulties encountered in specimen preparation, and it is, thus, advisable to consider these two transverse sections as a single set when attempting to formulate the true structure of the scale layers.

The results of an EDS analysis of the transverse section shown in Fig. 13(a) are summarized in Table 10. Here, it is seen that the outer scale layer contains essentially only chromium and manganese as metallic elements and, in parallel with the earlier data for specimen AR1 (24-h exposure), most probably represents a $(\text{Mn,Cr})_3\text{O}_4$ -type spinel product. Also, in parallel with that earlier set of observations, the inner scale layer is likely a distorted Cr_2O_3 compound. It is also

Table 9. X-ray diffraction data for specimen AR1 after 24-h exposure in air at 900°C

Diffraction data (austenitic matrix)			JCPDS card 33-397 (chromium iron nickel)		
Strong components					
2 θ	d (Å) ^a	I/I ₀ ^b	(hkl)	d (Å) ^a	I/I ₀ ^b
43.674	2.0709	14	(111)	2.075	100
50.847	1.7943	10	(200)	1.796	45
74.797	1.2683	100	(220)	1.269	26
90.781	1.0820	18	(311)	1.082	30
Not scanned-----			(222)	1.037	12
Not scanned-----			(400)	0.898	3
Diffraction data (spinel oxide scale)			JCPDS card 10-319 (MnFe ₂ O ₄)		
2 θ	d (Å) ^c	I/I ₀ ^d	(hkl)	d (Å) ^c	I/I ₀ ^d
18.058	4.9084	12	(111)	4.906	20
29.680	3.0075	34	(220)	3.005	35
34.935	2.5662	100	(311)	2.563	100
36.592	2.4537	5	(222)	2.450	12
42.356	2.1322	27	(400)	2.124	25
52.678	1.7361	5	(422)	1.734	20
56.038	1.6397	24	(511)	1.635	35
61.616	1.5040	19	(440)	1.503	40
Sesquioxide interference			(531)	1.437	4
Not detected-----			(620)	1.344	4
72.820 ^e	1.2978	8	(533)	1.296	20
Austenite interference			(622)	1.281	15
Not detected-----			(444)	1.227	10
Not detected-----			(711)	1.190	12
85.557 ^e	1.1342	2	(642)	1.135	7
88.035	1.1085	4	(553)	1.106	30
Not detected-----			(800)	1.062	14

Table 9. (Continued)

Diffraction data (sesquioxide scale)			JCPDS card 35-1112 (Cr _{1.3} Fe _{0.7} O ₃)		
Medium components					
2 θ	d (Å) ^c	I/I ₀ ^f	(hkl)	d (Å) ^c	I/I ₀ ^f
24.337	3.6543	42	(012)	3.654	45
33.387	2.6816	31	(104)	2.676	100
35.891	2.5001	100	(110)	2.499	75
Not detected	-----	-----	(006)	2.270	4
41.238	2.1874	21	(113)	2.189	25
Austenite interference			(202)	2.063	4
49.881	1.8267	21	(024)	1.827	35
54.520	1.6818	23	(116)	1.680	65
57.963 ^g	1.5898	4	(122)	1.590	5
57.963 ^g	1.5898	4	(010)	1.585	6
62.952	1.4753	13	(214)	1.474	25
64.475	1.4429	27	(300)	1.442	25
Not detected	-----	-----	(208)	1.338	1
72.820 ^e	1.2978	15	(10:10)	1.299	12
76.227	1.2480	9	(220)	1.249	6
Not detected	-----	-----	(306)	1.218	3
Not detected	-----	-----	(128)	1.179	2
Not detected	-----	-----	(02:10)	1.152	4
85.552 ^e	1.1342	5	(134)	1.132	7
Not detected	-----	-----	(226)	1.095	7

^aa₀ = 3.558 Å; V.Strong (110) texture.

^bI₀ = 17271 cpm.

^ca₀ = 8.51 Å.

^dI₀ = 13311 cpm. Spinel is highly strained and has a large grain size.

^eLine shared by spinel and sesquioxide.

^fI₀ = 6804 cpm; exhibits some (110 texture). Sesquioxide is strained and had a large grain size.

^gSingle, very broad line assigned both reflections.

Note: No silica or silicate was detected.

Y210622

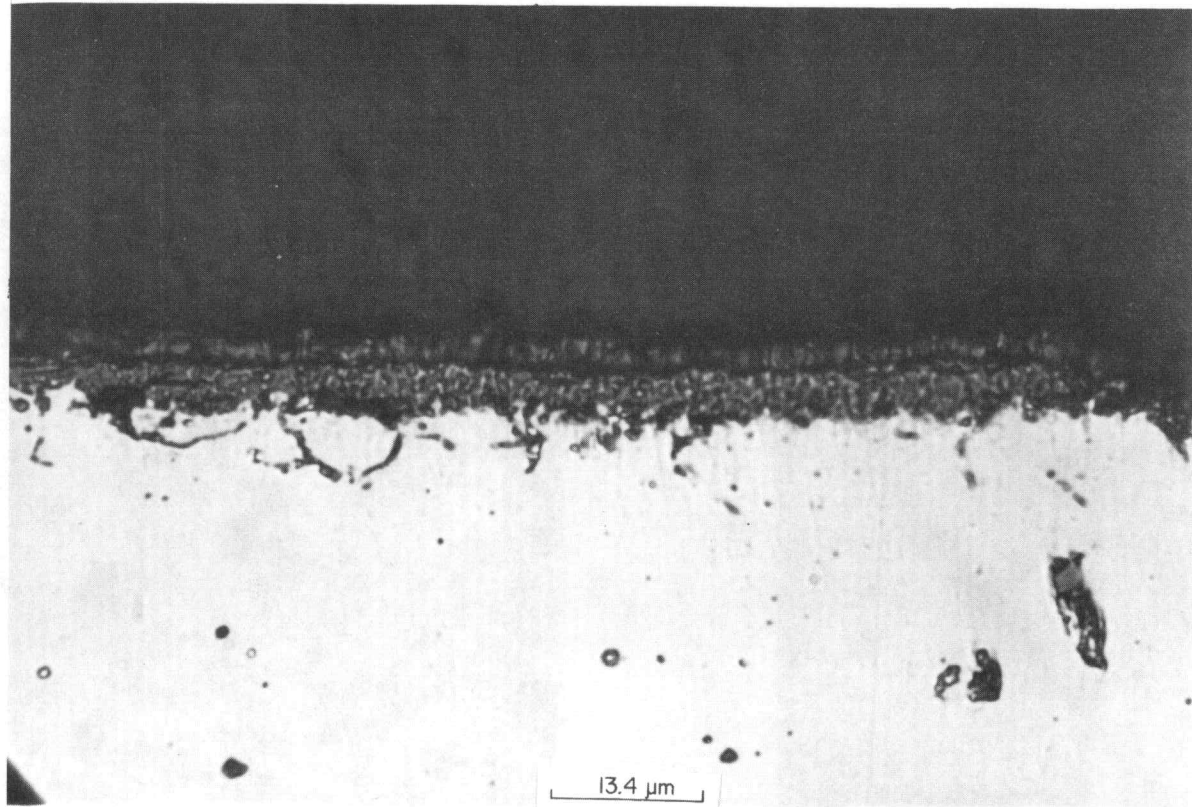
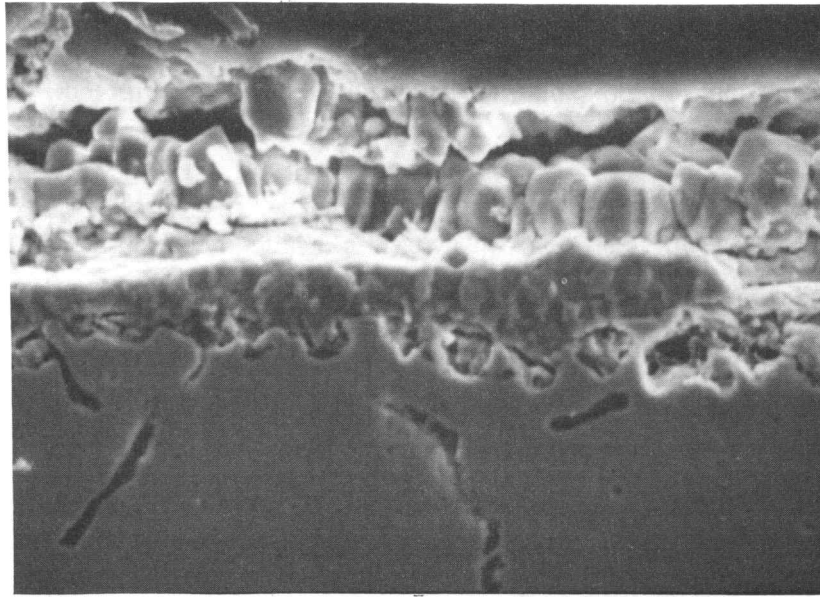


Fig. 12. Photomicrograph of a transverse section of etched specimen AR4 after 216-h exposure in air at 900°C.

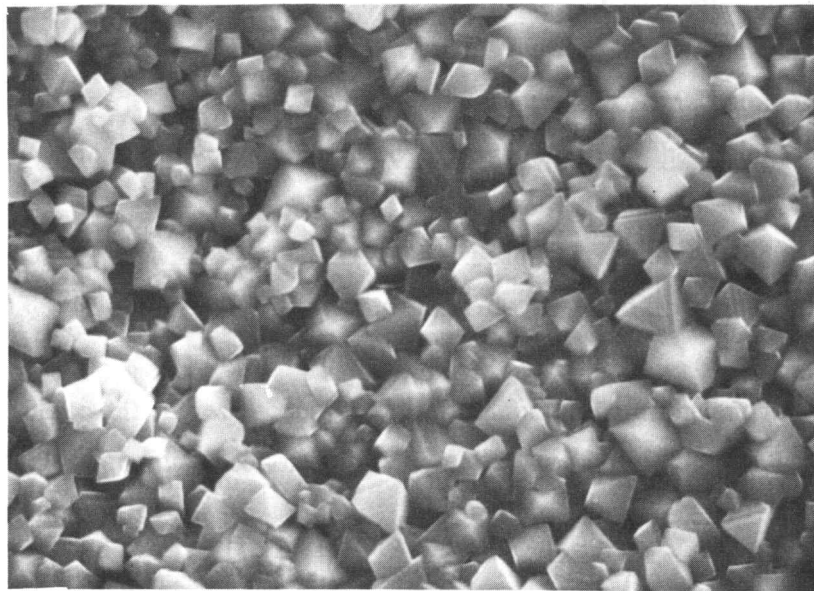
M27564



(a)

 $1.00 \mu\text{m}$

M27558



(b)

 $1.00 \mu\text{m}$

Fig. 13. Electron micrographs showing the scale structure of specimens AR4 and AR5, respectively, after exposure in air at 900° C: (a) transverse section after 216 h and (b) external surface after 384 h.

**Table 10. Qualitative EDS analysis for specimen AR4
after 216-h exposure in air at 900° C
(summary of relative elemental abundance)^a**

Chemical element	Position in transverse section ^b			
	(A)	(B)	(C)	(D)
Iron	100	100	1	0
Chromium	67	54	100	100
Nickel	27	25	0.2	0
Manganese	0.4	0.6	0.2	52
Silicon	0.9	0.8	0.4	0.6

^aRelative elemental abundance is in terms of each elements K- α excitation divided by that for the strongest element (presented as percentages).

^bKey to positions:

- (A): Denuded zone distal from the alloy-oxide interface.
- (B): Denuded zone proximal to the alloy-oxide interface.
- (C): Inner scale layer; nearest alloy-oxide interface.
- (D): Outer scale layer; nearest gas-oxide interface.

noted that the denuded zone, immediately below the scale, is somewhat poorer in chromium than the bulk alloy, as may be expected if chromium is utilized in the scale-building process.

The qualitative chemistries for the inner and outer scale layers closely parallel those obtained from the transverse section, Table 10. A feature of this analysis, also observed for several other specimens, was a mound-like rosette of idiomorphic crystals, which were extremely rich in titanium. It is believed that such growths originated from "tramp" titanium in the alloy. Because these mounds are many times seen in linear arrays, it is believed that the titanium initially formed as carbides that were subsequently drawn into the form of particle strings by the metalworking practice. Due to the very high affinity of titanium for oxygen, the carbides were subsequently oxidized to produce a very low areal density of such mounds.

This description of the scale is reinforced by data gathered from an EDS analysis done on the external surface of the scale and summarized in Table 11.

Table 11. Qualitative EDS analysis for specimen AR4 after 216-h exposure in air at 900° C (summary of relative elemental abundance)^a

Chemical element	Feature in normal section ^b		
	(A)	(B)	(C)
Iron	0	2	0
Chromium	100	100	47
Nickel	0	0.5	0
Manganese	42	3	20
Silicon	0	0.7	0
Titanium	0	0	100

^aRelative elemental abundance is in terms of each element's k- α excitation divided by that for the strongest element (presented as percentages).

^bKey to positions:

- (A): Outermost surface of the scale layers.
- (B): Inner scale layer as exposed by local spalling.
- (C): Localized rosette mound of idiomorphic crystals.

At the longest test period investigated, 384 h (16 d), the outermost surface of the scale matures into relatively large, faceted, nodular crystals. As shown in Fig. 13(b), some of these crystals exhibit an octahedral morphology as would be expected in the formation of a spinel-type structure. Such was confirmed by X-ray diffraction as shown in Table 12 below. Here, it is seen that the strongest portion of the pattern does, indeed, arise from spinel structures, with a weaker Cr_{1.3}Fe_{0.7}O₃ pattern evidently being evolved from the inner scale layer. Of special interest in this analysis is that two, rather than one, spinels have formed in this late stage of scale growth. This is suggestive of an incongruent solid-state reaction occurring within the spinel phase as time progresses. It is possible that such reaction is encouraged by chemical gradients that occur within the scale and arise, fundamentally, from the fact that the chemical fluxes during the initial portion of oxidation may be grossly different from those that occur later.

Table 12. X-ray diffraction data for specimen AR6 after 384-h exposure in air at 900°C (File CT357C)

Diffraction data (spinel oxide scale)			JCPDS card 10-319 (MnFe ₂ O ₄)		
Strong components					
2 θ	d (Å) ^a	I/I ₀ ^b	(hkl)	d (Å) ^a	I/I ₀ ^b
Not scanned-----			(111)	4.906	20
29.722	3.0034	33	(220)	3.005	35
34.981	2.5630	100	(311)	2.563	100
36.681	2.4480	6	(222)	2.450	12
42.513	2.1247	31	(400)	2.124	25
52.765	1.7335	6	(422)	1.734	20
56.190	1.6357	27	(511)	1.635	35
61.774	1.5005	24	(440)	1.503	40
Sesquioxide interference			(531)	1.437	4
70.104	1.3412	2	(620)	1.344	4
73.117 ^c	1.2932	4	(533)	1.296	20
73.981	1.2802	2	(622)	1.281	15
77.855	1.2259	1	(444)	1.227	10
Not detected-----			(711)	1.190	12
85.655 ^c	1.1331	3	(642)	1.135	7
88.354	1.1053	4	(553,731)	1.106	30
92.768	1.0640	2	(800)	1.062	14
100.690	1.0005	1	(660)	Not listed	X
103.6834	0.9796	2	(555,751)	0.982	20
104.3477	0.9752	1	(662)	Not listed	X
108.0566	0.9518	2	(840)	Not listed	X
Diffraction data [spinel oxide scale (ghost)]			JCPDS card 10-319 (MnFe ₂ O ₄)		
2 θ	d (Å) ^d	I/I ₀ ^b	(hkl)	d (Å) ^d	I/I ₀ ^b
Reads on primary spinel at all higher "d-values."					
70.387 ^c	1.3365	1	(620)	1.344	4
73.394	1.2890	2	(533)	1.296	20
74.233	1.2765	2	(622)	1.281	15
78.214	1.2212	1	(444)	1.227	10
Not detected-----			(711)	1.190	12
85.793	1.1317	3	(642)	1.135	7
88.543	1.1035	4	(553,731)	1.106	30
93.330	1.0590	2	(800)	1.062	14
Not detected-----			(660)	Not listed	X
Not detected-----			(555,751)	0.982	20
Not detected-----			(662)	Not listed	X
109.3002	0.9444	2	(840)	Not listed	X

Table 12. (Continued)

Diffraction data (sesquioxide scale)			JCPDS card 35-1112 (Cr _{1.3} Fe _{0.7} O ₃)		
Medium components					
2 θ	d (Å) ^d	I/I ₀ ^e	(hkl)	d (Å) ^d	I/I ₀ ^e
24.315	3.6576	19	(012)	3.654	45
33.359	2.6838	13	(104)	2.676	100
35.870	2.5015	100	(110)	2.499	75
Not detected	-----	-----	(006)	2.270	4
41.195	2.1896	17	(113)	2.189	25
43.759	2.0670	5	(202)	2.063	4
49.881	1.8268	21	(024)	1.827	35
54.493	1.6825	19	(116)	1.680	65
57.913	1.5911	6	(122)	1.590	5
Not detected	-----	-----	(010)	1.585	6
62.976	1.4748	19	(214)	1.474	25
64.525 ^c	1.4430	54	(300)	1.442	25
70.387	1.3365	4	(208)	1.338	1
73.117 ^c	1.2932	14	(10:10)	1.299	12
76.188	1.2485	11	(220)	1.249	6
78.312	1.2199	5	(306)	1.218	3
81.488	1.1807	6	(128)	1.179	2
Not detected	-----	-----	(02:10)	1.152	4
85.655	1.1331	11	(134)	1.132	7
89.473	1.0944	6	(226)	1.095	7
Diffraction data (austenitic matrix)			JCPDS card 33-397 (chromium iron nickel)		
2 θ	d (Å) ^f	I/I ₀ ^g	(hkl)	d (Å) ^f	I/I ₀ ^g
43.591	2.0746	498s	(111)	2.075	100 3.593
50.752	1.7974	471s	(200)	1.796	45 3.595
74.698	1.2697	7091s	(220)	1.269	26 3.591
90.730	1.0825	1810s	(311)	1.082	30 3.590
Not detected	-----	0	(222)	1.037	12
Not detected	-----	0	(400)	0.898	3

^aa₀ = 8.50 Å; spinel has line broadening.

^bI₀ = 30824 cpm.

^cLine shared by spinel and sesquioxide.

^da₀ = 8.46 Å; spinel has line broadening.

^eI₀ = 8290 cpm; exhibits some (110) texture.

^fa₀ = 3.592 Å; V.Strong (110) texture.

^gI₀ = 7091 cpm..

The exact chemical nature of these spinels has not been determined here; however, one of them is probably of the $(\text{Mn,Cr})_3\text{O}_4$ as has been suggested above.

3.3 "LEAN" SULFIDIZING ATMOSPHERES

Five tests were run in the "lean" sulfidizing atmosphere at temperatures of 800, 900, and 1000°C using both flat and ell-shaped specimens. Their purpose was to determine: (1) the kinetics of the reaction; (2) qualitatively, the magnitude of the stresses generated during the oxidation process; and (3) structural information regarding the reaction products that were formed.

At 900°C, the rate of oxidation was found to be essentially parabolic subsequent to an initial transient period during which the rate was more rapid. This behavior is shown in Fig. 14, from which the effective parabolic rate constant was determined to be $1.11 \times 10^{-3} \text{ mg}^2\text{cm}^{-4}\text{h}^{-1}$. This rate was approximately equal to that experienced in air at 800°C and more than 3 times smaller than that found for the baseline tests run in air at 900°C. As sulfur was not overtly involved in compound formation upon these specimens (described below), the reduction in rate is most probably associated with the 10^6 times lower oxygen partial pressures involved in these tests (Appendix I). As in the case of oxidation in air, no sensible spalling or evidence of scale breakdown was noted for these specimens.

The deformations suffered by ell-shaped specimens as a result of exposure to the "lean" sulfidizing atmosphere at 800 and 900°C differed grossly from those exposed in air. At 800°C, neither angle closure nor dilatation was observed; while at 900°C, the angles of the ells increased and the dilatations were very small. These dimensional changes for the 900°C exposures are summarized in Table 13 below. Because weak dilatations of the gage lengths were found and because its rate appears to be related to the parabolic reaction, it is presumed that the opening of the ells is primarily a creep-related phenomenon induced by gravitational effects. Had these mechanical deformations been directly related to the amount of scale formation, then, by calculation, one would have expected an angle closure of approximately 15° and a dilatation of approximately 1% after 24 h of exposure in the sulfidizing atmosphere. As the observed values were very much smaller, it is concluded that the cooperative, tractive forces between the scale and its alloy substrate are greatly diminished, if not completely absent, in the "lean" sulfidizing atmosphere. For the latter case, the small dilatations that were observed may arise from phenomena as oxygen solution in the alloy, oxide formation within the alloy or scale, etc.

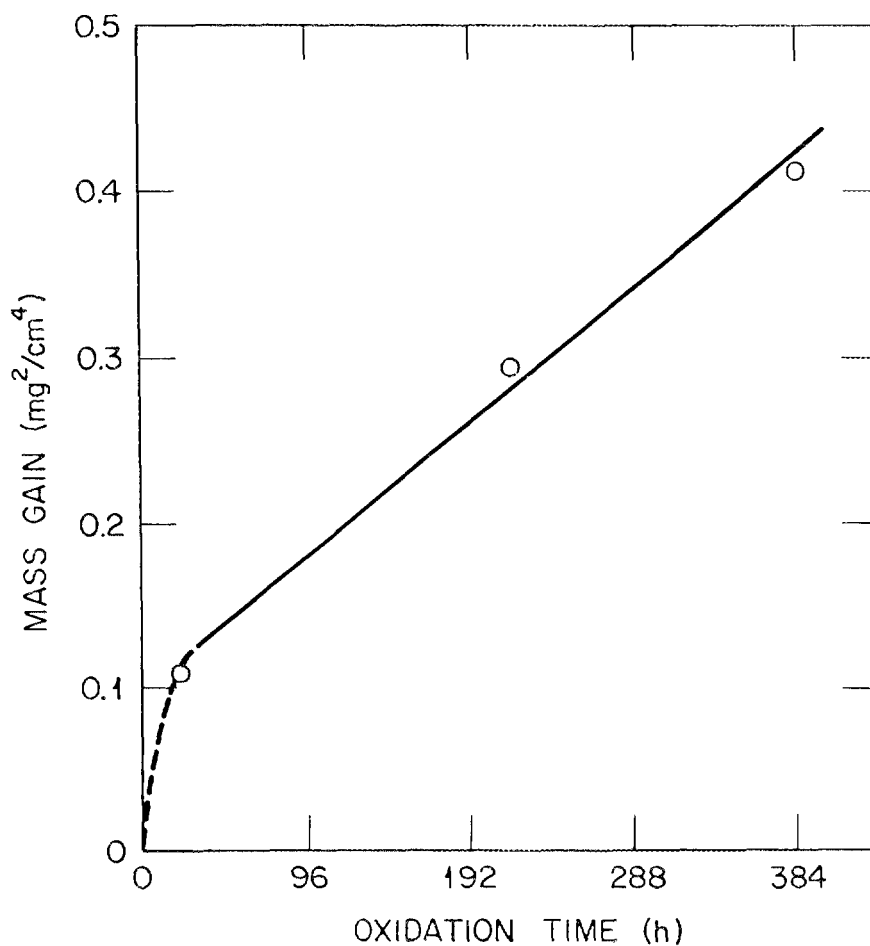


Fig. 14. Square of specific mass gain as a function of time for specimens exposed in the "lean" sulfidizing atmosphere at 900°C.

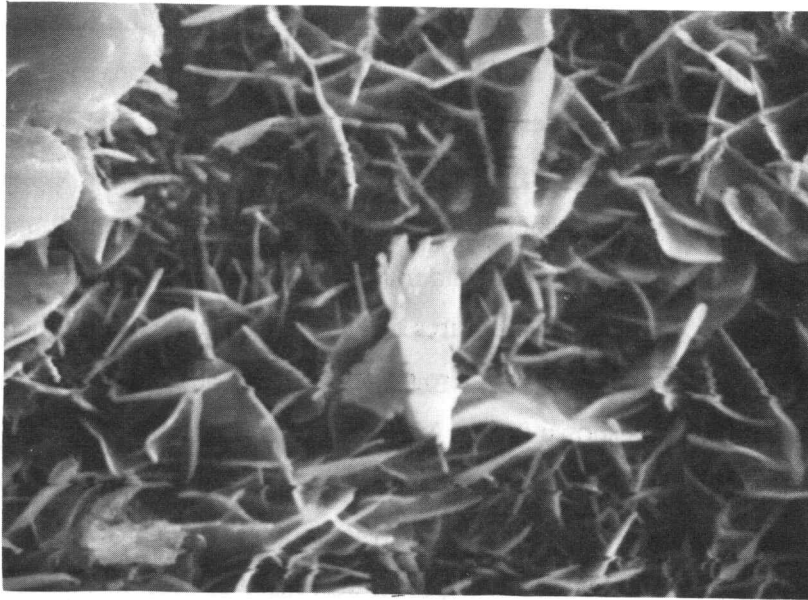
Table 13. Deformation of ell-shaped specimens in the "lean" sulfidizing atmosphere at 900°C

Specimen number	Exposure time (h)	Angle closure (deg)	Closure rate (deg/h ^{1/2})	Dilatation	
				Linear (%)	Rate (h ^{1/2})
E1R5	24	-4.0	-0.82	0.23	0.047
E1R6	216	-6.0	-0.41	0.38	0.026
E1R7	384	-9.5	-0.48	0.80	0.041

The structural aspects of the scales formed in the "lean" sulfidizing atmosphere also differed markedly from those formed in air. The most striking aspect was the formation of blade-like products as seen from the gas-oxide interface of the scales. Two photographs, which represent what are essentially the limiting cases of this structural aspect, are shown in Fig. 15 for 24-h exposures at 800 and 1000°C. At the lower temperature, Fig. 15(a), the visible portion of the product is almost totally bladelike, whereas at the higher temperature, small blades are admixed with nodules and, in a few selected areas, mounds of product involving ribbon-like growths are seen as shown in Fig. 15(b). That the structures of Fig. 15 represent extremes in reaction product evolution is reinforced by a similar set of micrographs of scales obtained from specimens exposed for 24 and 384 h at 900°C, as shown in Fig. 16. For the earlier time [Fig. 16(a)], the structure is predominantly bladelike; however, upon close inspection, one may discern small nodules having formed between the blades. For the longer time, the nodules dominate the structure, either the size or the areal density of the blades having been decreased as seen in Fig. 16(b). In addition, that photograph shows one of the ribbon-like growths noted earlier for the 1000°C exposure.

The average (integrated) surface and product blade chemistries of these scales, developed after 24 h of reaction, are summarized in Table 14. It is seen that the surface is chromium-rich for all exposures with manganese again participating in the formation of reaction products, especially at the higher temperatures. The presence of sulfur is also noted; however, it is not known with certainty whether it appears as part of the scale or as a sulfate contamination due to the manipulation of specimens during or after their exposure. The presence of manganese may be associated with the development of the nodular product. The blade and average surface chemistries are similar, but the temperature dependence of the manganese concentration for the blades is inverse to that for the average surfaces. This suggests that manganese is to be associated with blade formation at the lower temperature, or early in the scale evolution, and that later on, or at higher temperatures, some of the manganese leaves the blade sites to develop the nodular product. The concept of manganese-rich nodules was reinforced by EDS examination of the specimens exposed long term at 900°C. The relative abundance of manganese in the overall scale was found to increase from 22 to 47 to 64 as the exposure times increased from 24 to 216 to 384 h. Further, the relative abundances of manganese and chromium in the nodules per se were found to be 100 and 53 after the 216-h exposure. It is therefore concluded that manganese is to be associated with the nodular morphology observed here.

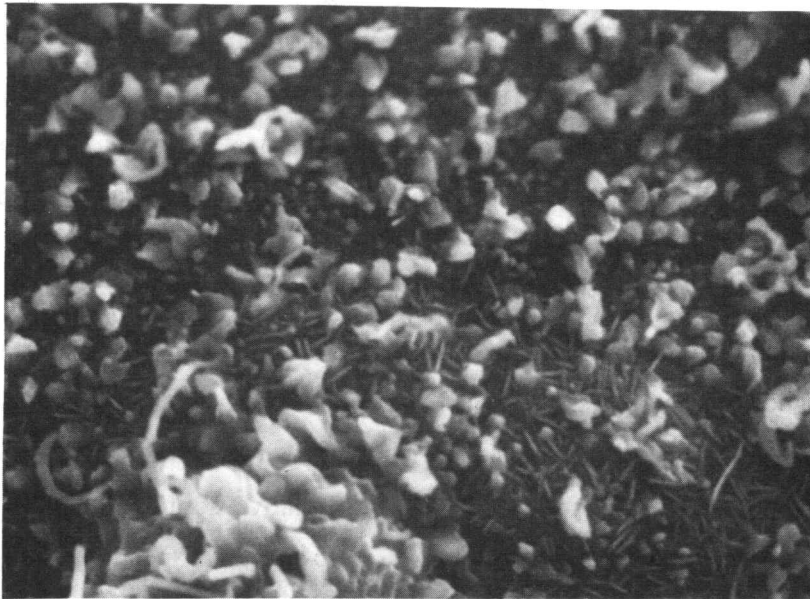
M27309



(a)

1.00 μm

M27594

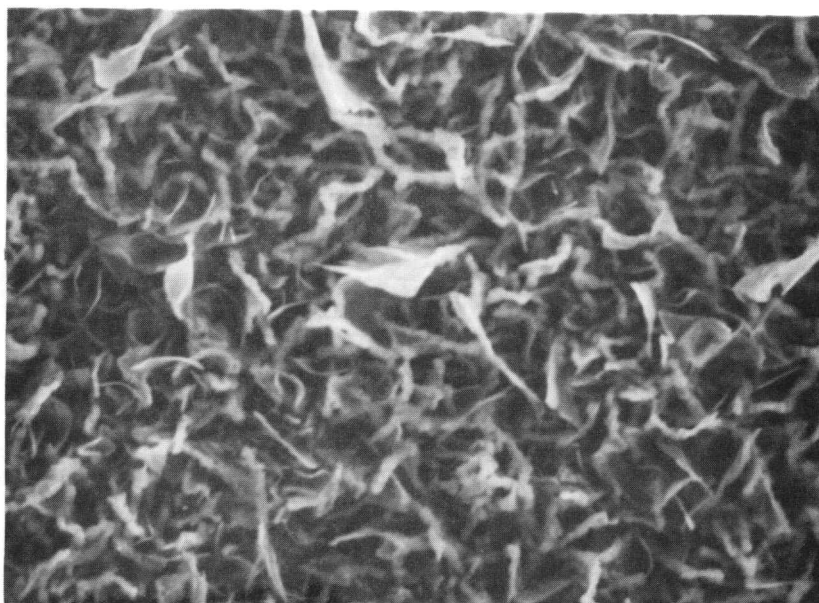


(b)

1.00 μm

Fig. 15. Electron micrographs showing the scale structure of specimens E1R4 and AR8 after exposure in the "lean" sulfidizing atmosphere: (a) Surface after 24 h at 800° C and (b) surface after 24 h at 1000° C.

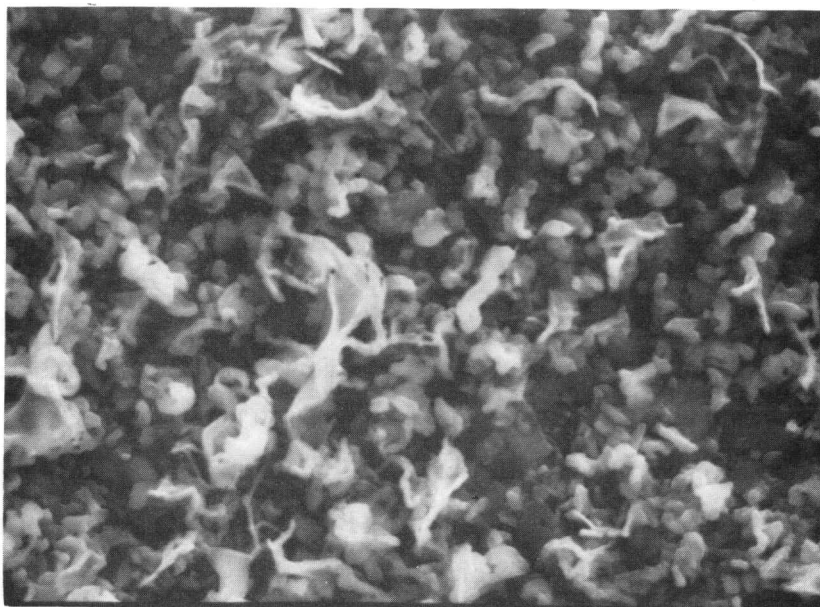
M27673



(a)

 $1.00 \mu\text{m}$

M27392



(b)

 $1.00 \mu\text{m}$

Fig. 16. Electron micrographs showing the scale structure of specimens E1R5 and E1R7 after exposure in the "lean" sulfidizing atmosphere at 900° C: (a) Surface after 24 h and (b) surface after 384 h.

Table 14. Qualitative EDS analyses for specimens E1R4, E1R5, and AR8 after 24-h exposure in the "lean" sulfidizing atmosphere (summary of relative elemental abundance)^a

Chemical element	800° C	900° C	1000° C
Average surface density			
Iron	3	4	1.9
Chromium	100	100	100
Nickel	0.8	2	0.4
Manganese	3	22	29
Silicon	2.5	0.7	0
Titanium	0	0	2.7
Sulfur	0	0	0.7
Product blade chemistry			
Iron	3	7	1.2
Chromium	100	100	100
Nickel	0	2	0.3
Manganese	24	15	9
Silicon	3	0.7	0.4
Titanium	0	0	1.1
Sulfur	1.6	0	0

^aRelative elemental abundance is in terms of each element's K- α excitation divided by that for the strongest element (presented as percentages).

Because the scale structure had evolved furthest on the specimen exposed at 1000° C, its surface was examined more intensively by the EDS technique. The chemistries of selected special surface features are summarized in Table 15.

Beneath a microscopic area of spalled scale was found an inner scale layer with featureless topography, which was apparently a chromia layer. Below it was the alloy substrate partially covered by various crystal types, some of which were very rich in titanium (which is involved in the production of the localized rosette structures cited earlier). This suggests that the spalled area may represent the base of a rosette mound that had fallen away. Such mounds were observed on this specimen, similar to those observed in air (Table 11). At the external surface of the scale were found the manganese- and chromium-rich ribbon and nodular idiomorphs in association with

Table 15. Qualitative EDS analysis for specimen AR8 after 24-h exposure in the "lean" sulfidizing atmosphere at 100° C (summary of relative elemental abundance)^a

Chemical element	Feature in normal section ^b			
	(A)	(B)	(C)	(D)
Iron	14	100	1.1	1.7
Chromium	100	95	32	92
Nickel	3.7	24	0.4	0
Manganese	1.7	0.4	100	100
Silicon	1.8	2.8	2.2	1.0
Titanium	0	39	0	0
Sulfur	0	0	3.8	1.7

^aRelative elemental abundance is in terms of each element's K- α excitation divided by that for the strongest element (presented as percentages).

^bKey to positions:

- (A): Inner scale layer as revealed by local spalling.
- (B): Material beneath inner scale layer; same spall area.
- (C): Ribbon-like crystals on the outer scale layer.
- (D): Nodular crystals on the outer layer scale.

relatively small amounts of sulfur. The sulfur signal is much too weak to be representative of sulfides; yet, these idiomorphs contain sulfur concentrations up to five times that of the scale, in general, and thus represent sulfur "hot spots." The role that sulfur plays in this instance is unclear.

An X-ray diffraction analysis of the specimen exposed to the "lean" atmosphere for 24 h at 900° C indicated the very strong presence of Cr₂O₃ (undistorted) and less intense patterns representing the spinels Mn_{1.5}Cr_{1.5}O₄ and MnFe₂O₄ (Table 16). In view of the chemical data for this specimen (see Table 16), it is more probable that the latter spinel is again actually of the (Mn,Cr)₃O₄ type. Another analysis conducted on the specimen similarly exposed at 800° C also indicated that chromia and only the Mn_{1.5}Cr_{1.5}O₄ spinel were present; that diffraction pattern is not documented here.

To further understand the details of the scale structure developed in the "lean" sulfidizing atmosphere, a transverse section of the specimen exposed for 216 h was prepared and examined. The micrographs of that section, illustrating the two-layer scale, are shown in Fig. 17. Of special

Table 16. X-ray diffraction data for specimen E1R5 after 24-h exposure in "lean" sulfidizing atmosphere at 900° C

Diffraction data (austenitic matrix)			JCPDS card 33-397 (chromium iron nickel)		
Strong components					
2 θ	d (Å) ^a	I/I ₀ ^b	(hkl)	d (Å) ^a	I/I ₀ ^b
43.719	2.0689	30	(111)	2.075	100
50.908	1.7923	19	(200)	1.796	45
74.811	1.2681	100	(220)	1.269	26
90.814	1.0817	15	(311)	1.082	30
96.115	1.0356	2	(222)	1.037	12
118.258	0.8974	1	(400)	0.898	3
Diffraction data (sesquioxide scale)			JCPDS card 6-504 (Cr ₂ O ₃)		
2 θ	d (Å) ^c	I/I ₀ ^d	(hkl)	d (Å) ^c	I/I ₀ ^d
24.448	3.6380	30	(012)	3.633	75
33.472	2.6750	100	(104)	2.666	100
35.985	2.4937	49	(110)	2.480	95
39.526	2.2781	7	(006)	2.264	12
41.282	2.1852	16	(113)	2.176	40
Austenite			(202)	2.048	10
interference			(024)	1.816	40
50.361	1.8225	14	(116)	1.672	90
54.575	1.6802	46	(122)	1.579	14
Not detected	0		(214)	1.465	25
63.071	1.4728	10	(300)	1.431	40
64.575	1.4420	11	(10:10)	1.296	20
72.411	1.3041	8	(220)	1.240	18
76.186	1.2486	4	(306)	1.210	8
Not detected	0		(312)	1.173	14
Not detected	0		(02:10)	1.148	10
83.670	1.1549	4	(134)	1.124	10
85.860	1.1309	3	(226)	1.087	18
89.415	1.0950	4	(21:10)	1.042	16
94.704	1.0473	4			
Diffraction data (spinel oxide scale)			JCPDS card 35-1112 (Mn _{1.5} Cr _{1.5} O ₄)		
2 θ	d (Å) ^e	I/I ₀ ^f	(hkl)	d (Å) ^e	I/I ₀ ^f
Not scanned	-----	-----	(111)	4.88	25
29.8729	2.9886	72	5196d(220)	2.985	50 8.453

Table 16. (Continued)

Diffraction data (spinel oxide scale)			JCPDS card 35-1112 (Mn ₁₅ Cr ₁₅ O ₄)		
2 θ	d (Å) ^e	I/I ₀ ^f	(hkl)	d (Å) ^e	I/I ₀ ^f
35.157	2.5506	100	7260d(311)	2.545	100 8.459
36.849	2.4372	8	580d(222)	2.438	6 8.443
42.8574	2.1084	6	401p(400)	2.110	20 8.434
52.9394	1.7282	7	483p(422)	1.723	10 8.466
56.6250	1.6241	10	761d(511)	1.625	30 8.439
62.1796	1.4917	18	1300d(440)	1.493	45 8.438
Not detected-----			(533)	1.288	6
Austenite interference			(622)	1.273	2

Diffraction data (ghost spinel oxide scale)			JCPDS card 10-319 (MnFe ₂ O ₄)		
2 θ	d (Å) ^g	I/I ₀ ^h	(hkl)	d (Å) ^g	I/I ₀ ^h
42.4820	2.1262	10	735d(400)	2.124	25 8.505
Not detected-----			(422)	1.734	20
56.1039	1.6380	12	903d(511)	1.635	35 8.511
61.6980	1.5022	22	1631d(440)	1.503	40 8.498
Not detected-----			(531)	1.437	4
Not detected-----			(620)	1.344	4
Sesquioxide interference			(533)	1.296	20
Not detected-----			(622)	1.281	15
Not detected-----			(444)	1.227	10
Not detected-----			(711)	1.190	12
Not detected-----			(642)	1.135	7
88.467	1.1042	5	395s(553)	1.106	30 8.482

Lines of pattern NOT assigned

2 θ	d (Å)	I/I ₀
43.0813	2.0980	296
50.005	1.8105	413
88.467	1.1042	395
94.590	1.0482	512
96.115	1.0356	589

^aa₀ = 3.588 Å; V.Strong (110) texture.

^bI₀ = 30024 cpm.

^cEvidence for some (104) texture; not highly strained.

^dI₀ = 11601 cpm.

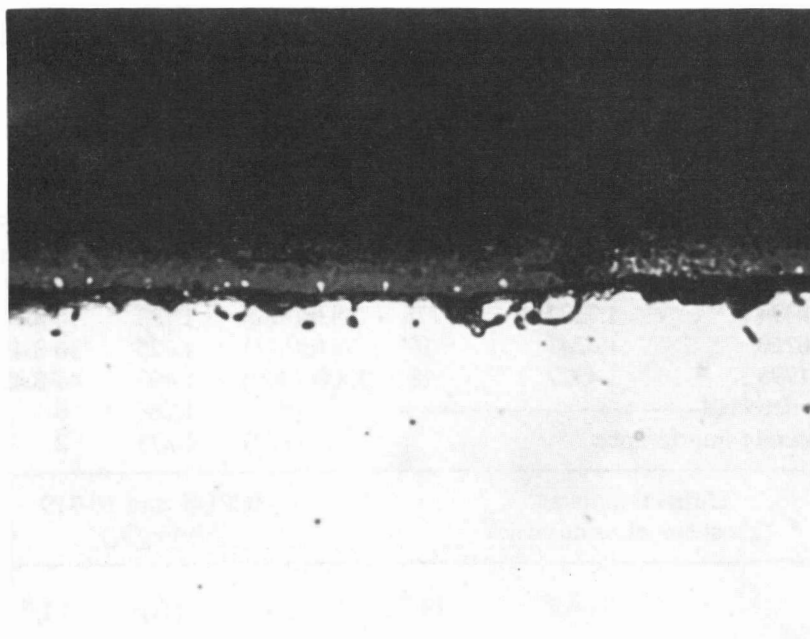
^ea₀ = 8.45 Å; strained and large grain size.

^fI₀ = 7260 cpm; apparently textured.

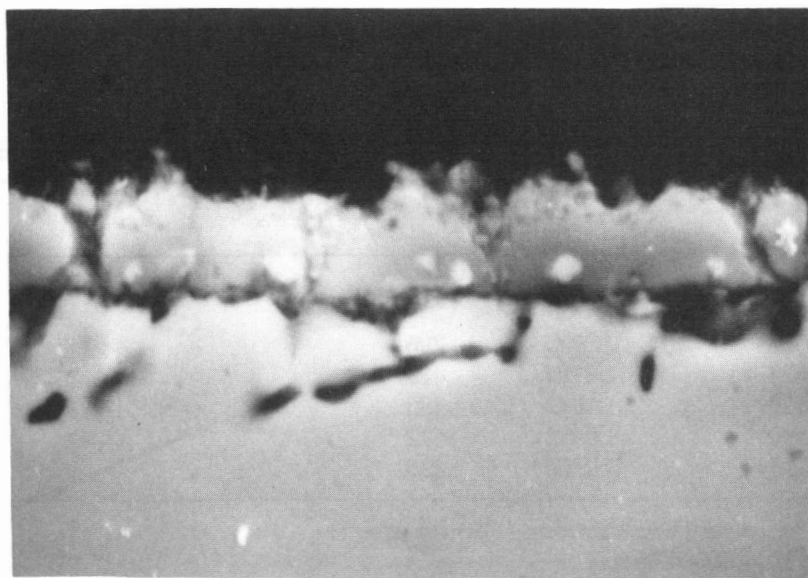
^ga₀ = 8.50 Å; strained and large grain size.

^hI₀ = 7260 cpm.

Note: Lines with larger "d-values" are not separable from above.



(a)



(b)

1.00 μm

Fig. 17. Micrographs of the transverse scale structure of specimen E1R6 after 216-h exposure in the "lean" sulfidizing atmosphere at 900°C: (a) Optical photomicrograph and (b) electron micrograph.

interest here are the bright and somewhat spherical particles embedded in the inner layer of scale near the metal-oxide interface. The fact that they appear bright in the electron micrograph of Fig. 17(b) indicates that they probably have a metallic character. The results of an EDS analysis of that transverse section are summarized in Table 17. The particles appear to be rich in chromium; however, this is believed to be an artifact due to signal "spillover" from the surrounding inner scale layer. Tentatively, these features are identified as mechanically enfolded austenite particles possibly originating from the encirclement of austenite grains by the sulfidation process as seems to be suggested in the photograph of Fig. 17(a). It is noted that no such structural feature was observed for the case of oxidation in air.

Table 17. Qualitative EDS analyses for specimen E1R6 after 216-h exposure in the "lean" sulfidizing atmosphere at 900° C (summary of relative elemental abundance)^a

Chemical element	Feature in transverse section ^b		
	(A)	(B)	(C)
Iron	30	2.1	0
Chromium	100	100	100
Nickel	9.0	0.8	0
Manganese	5.9	6.1	54
Silicon	2.0	1.1	1.9
Titanium	0	0	0
Sulfur	0	0	0

^aRelative elemental abundance is in terms of each element's K- α excitation divided by that for the strongest element (presented as percentages).

^bKey to positions:

- (A): Spheroidal metallic particle embedded in scale.
- (B): Inner scale layer near particle.
- (C): Outer scale layer.

In support of the prior discussions of scale structure, the data of Table 17 indicate that the inner scale layer is essentially Cr₂O₃, while the outer layer is probably a mixture of that chromia

and a spinel of mixed chemistry as: $(\text{Mn,Cr})_3\text{O}_4$. Combining this information with the scale topographies discussed earlier, it appears that the chromia forms first as vertical blades and later grows laterally to become a continuous inner layer. Subsequently, nodular crystals of spinel form between the blades, which are overgrown by it at still later times.

3.4 "RICH" SULFIDIZING ATMOSPHERES

Five tests were run in the "rich" sulfidizing atmosphere at the single temperature of 900°C using both flat and ell-shaped specimens. Their purpose was to determine: (1) the kinetics of the reaction; (2) qualitatively, the magnitude of the stresses generated during the oxidation process; and (3) structural information regarding the reaction products that were formed.

The results are relatively complex as the "rich" atmosphere reacts rapidly and extensively with the 310S substrate. After cooling and examination of the capsule contents, it was found that at least a portion of the reaction products had spalled. Mass gains were calculated based on both the reacted sample and spalled material. The kinetic behavior is illustrated in Fig. 18 for specimens exposed at times ranging from 2 to 24 h, again with data plotted in a parabolic format. The initial linear portion of that curve (shown dotted) represents a parabolic rate constant whose value is $2.20 \text{ mg}^2\text{cm}^{-4}\text{h}^{-1}$, a value some three orders of magnitude greater than that found for the "lean" sulfidizing atmosphere. The true reaction is believed to follow the sigmoidal curve represented by the solid line in Fig. 18. The decrease in the rate of reaction at the longest times is known to be associated with the near total consumption of the calcium sulfate - sulfur mixtures; thus, the fact that these data lie upon an extension of the dotted curve is purely fortuitous. In fact, the initial parabolic kinetics give way to some type of breakaway oxidation process at an exposure time near 5 h.

Only two of the specimens used in this series of tests were ell shaped and both of these exhibited an opening of the bend angle as was the case for the "lean" sulfidizing atmosphere. The values of dilatation for these specimens were also small, ranging from -0.3 to +0.1%; however, due to severe warpage of the specimens during reaction, the uncertainties in their measurement are equally large. As a result, it is concluded that, in this "rich" sulfidizing atmosphere, the cooperative tractive forces between the scale and its substrate are extremely weak (or nonexistent) and that one dominant mode of ell deformation involves creep induced by gravity. Because of the severe buckling of these specimens, it is clear that stress sources not simply related

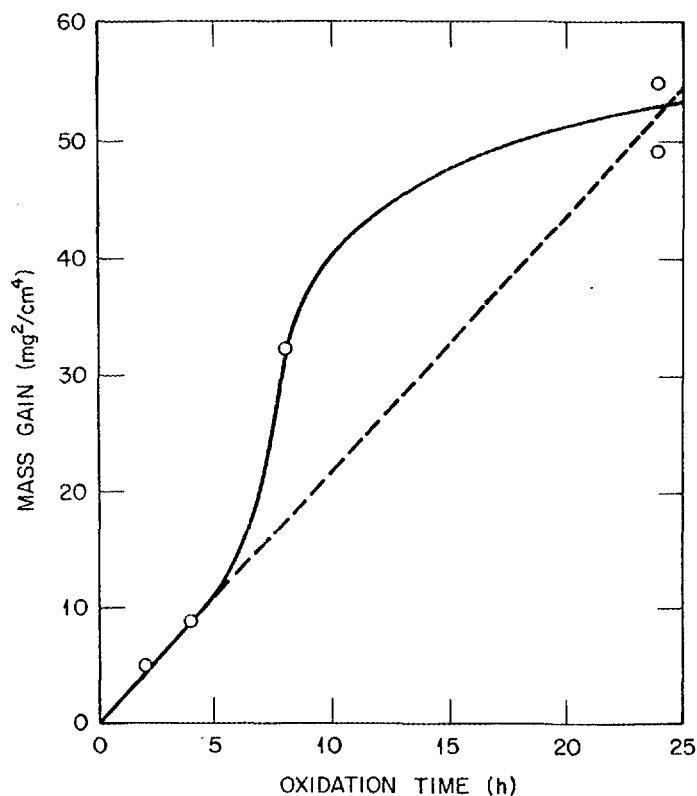


Fig. 18. Square of specific mass gain as a function of time for specimens exposed in the "rich" sulfidizing atmosphere at 900°C.

to the macroscopic geometry of the specimen are large and do come into play. The sources of these stresses are, as yet, undefined but may be related to internal compound formation or piece-wise, discontinuous adhesion of scale.

The complexity of the reaction, even at short times where the scale is relatively "protective," is underscored by the photomicrographs of Figs. 19 and 20, representing a specimen exposed for only 2 h. The transverse view of the specimen edge shown in Fig. 19 indicates that the scale forms thicker lobes at the specimen corners, which may arise from growth stresses. The scale shown there consists of at least two external layers with the innermost layer containing rounded and entrapped metallic particles. Immediately beneath the external scale is a second metallic layer that has entrapped particles of one of the reaction products, some of which, in turn,

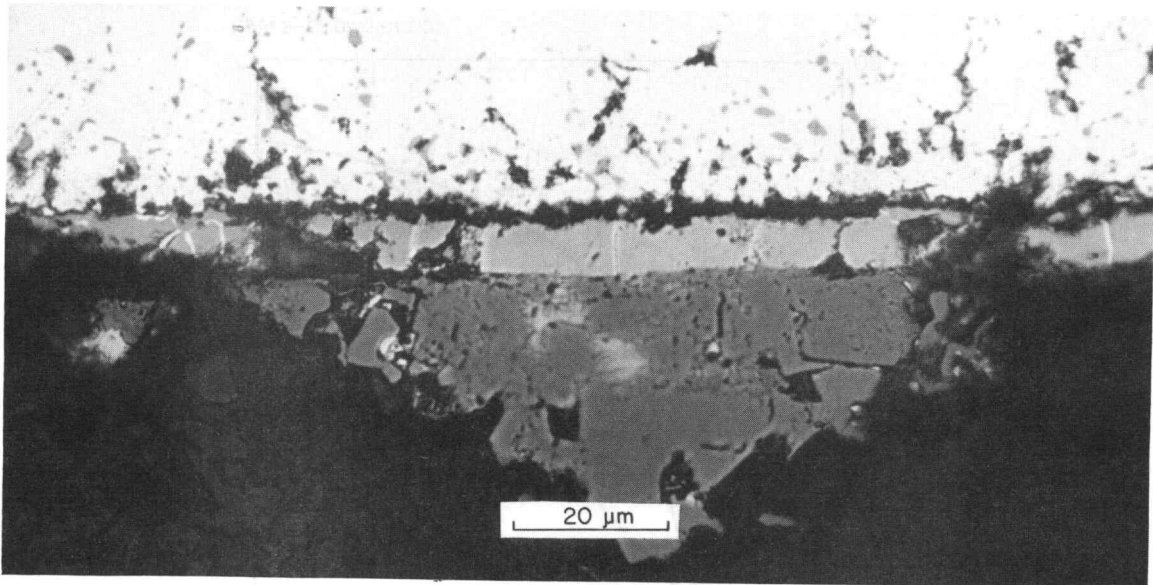


Fig. 19. Photomicrograph of a transverse section of specimen AR11 after 2-h exposure at 900°C in the "rich" sulfidizing atmosphere (Glyceresia etch).

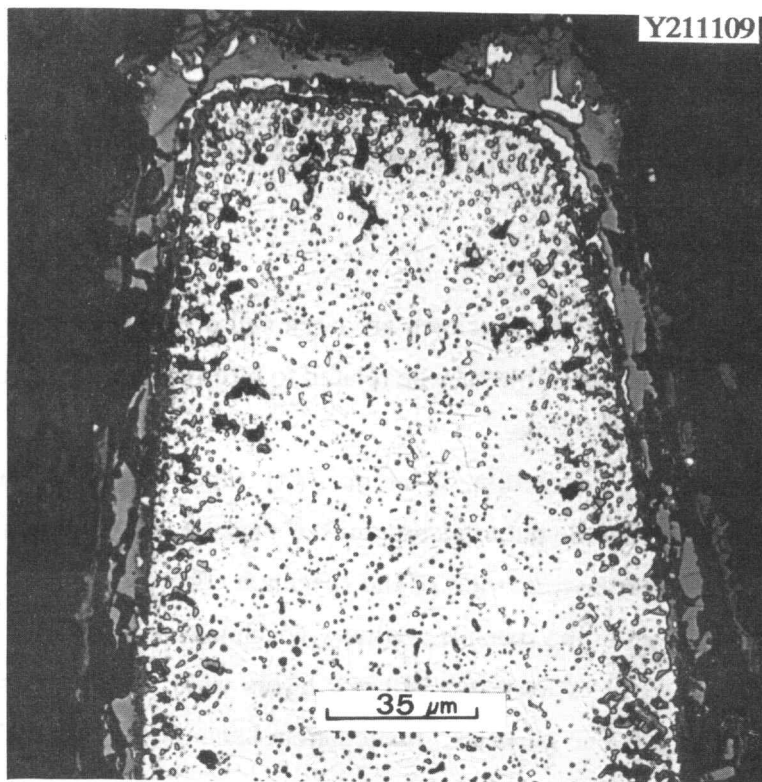


Fig. 20. Photomicrograph of as-polished transverse section of specimen AR11 after 2-h exposure at 900°C in the "rich" sulfidizing atmosphere.

contain voids. Further inward is a continuous layer of reaction product, which appears to be composed of particles sintered end to end. Beneath that layer are discrete, rounded particles of reaction product, some of which appear to be aligned along the substrate alloy grain-boundary network and many of which exhibit internal voids. Finally, the alloy's sigma phase decorates the interior of the specimen. It is strongly suspected that a low-melting sulfide was present as a liquid at temperature, and at least some of the void space observed is associated with the solidification shrinkage of that sulfide.

At occasional sites along the edge of that specimen exist protrusions such as that shown in Fig. 20. Here, one sees at least three scale layers: the outermost being nearly structureless and blocky; the central one containing some porosity, some metallic particles, and some trapped second phase; and an inner layer that is essentially featureless, except that it is veined, normal to the alloy-scale interface, by a thin, light-colored phase. The veins of this innermost layer are believed to be a re-solidified sulfide, as are the subscale particles (the sigma phase is not revealed here since no etchant was used).

At longer sulfidation times, the features of the structure coarsen and are, therefore, somewhat more amenable to analysis. Thus, Fig. 21 shows neatly separated layers representing what is believed to be three of the inner suite of the scale layers developed after 24 h of exposure. The innermost of these layers again exhibits a vein-like pattern, which, in this case, traverses all of the scale layers shown. An outer series of layers, initially present, has spalled away and its position is now replaced by that of the mounting material. The results of an EDS analysis of the same area as that shown in Fig. 21 are presented in Table 18.

The protrusions appear to be chromium-depleted austenite particles that lie upon an oxide layer rich in chromium, iron and manganese. The central scale layer appears to be composed of an essentially pure chromia. The innermost scale layer and the subscale particles appear to be chromium and mixed-metal sulfides, respectively. Thus, sulfides reside primarily in the region of the metal-scale interface insofar as this inner suite of scale layers is concerned.

At occasional sites on the surface of this specimen, it was possible to observe both the inner and outer suites of scale layers. These observations are brought together in Fig. 22 where electron micrographs taken using a 55° tilt angle are presented. It is seen that the overall scale is composed of at least six identifiable layers. The fine granular layer shown at the bottom of Fig. 22(b) has the same sulfur-rich chemistry as was displayed by the innermost scale layer of Fig. 21 (column D, Table 18). The results of EDS analyses on the outer suite of scale layers, shown in Fig. 22(a), are presented in Table 19.

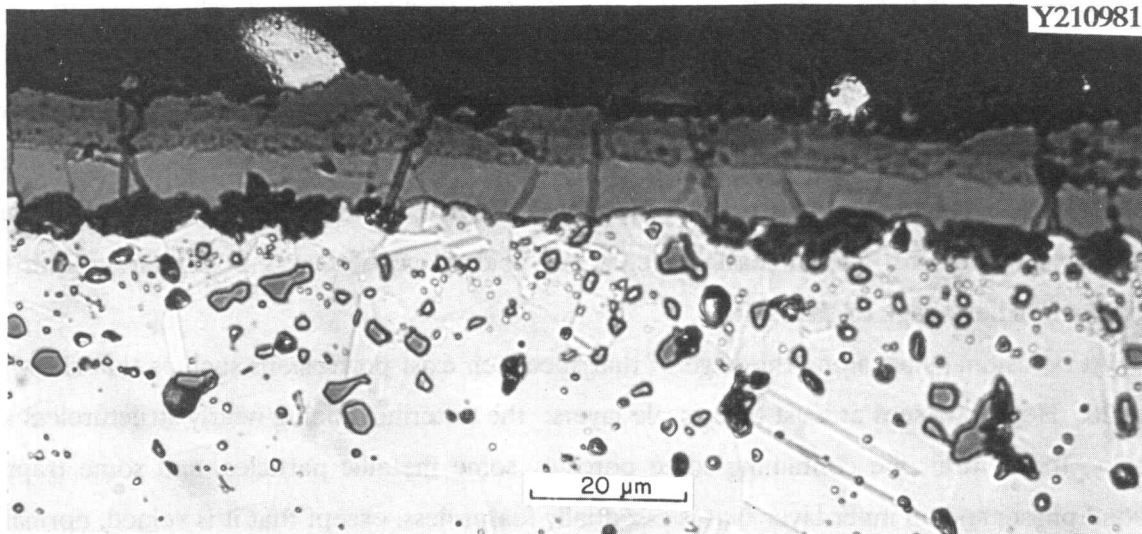


Fig. 21. Photomicrograph of etched transverse section of specimen E1R8 after 24-h exposure at 900°C in the "rich" sulfidizing atmosphere.

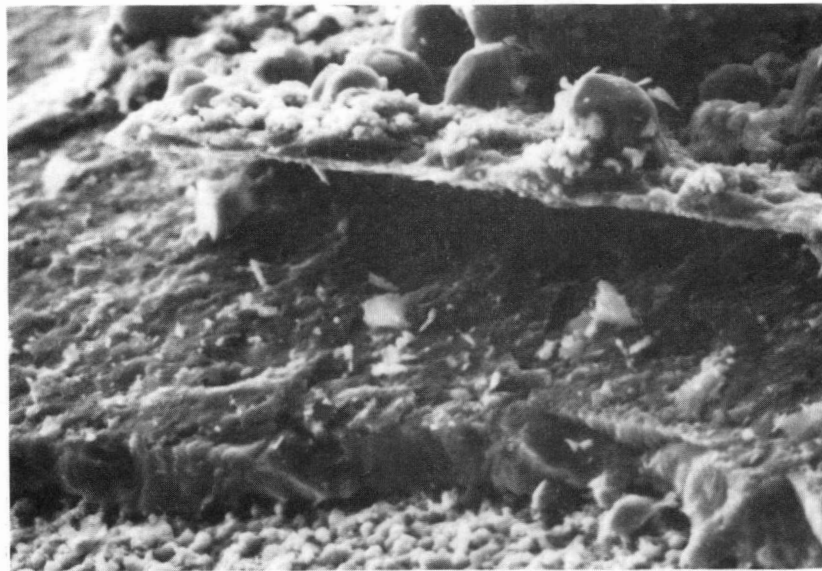
Table 18. Qualitative EDS analyses for specimen E1R8 after 216-h exposure in the "rich" sulfidizing atmosphere at 900°C (summary of relative elemental abundance)^a

Chemical element	Feature in transverse section ^b				
	(A)	(B)	(C)	(D)	(E)
Iron	100	50	7.3	1.1	82
Chromium	3.0	100	100	100	100
Nickel	32	0	0	0	14
Manganese	0.1	21	6.2	2.4	31
Sulfur	0	0	0	79	77

^aRelative elemental abundance is in terms of each element's K- α excitation divided by that for the strongest element (presented as percentages).

^bKey to positions:

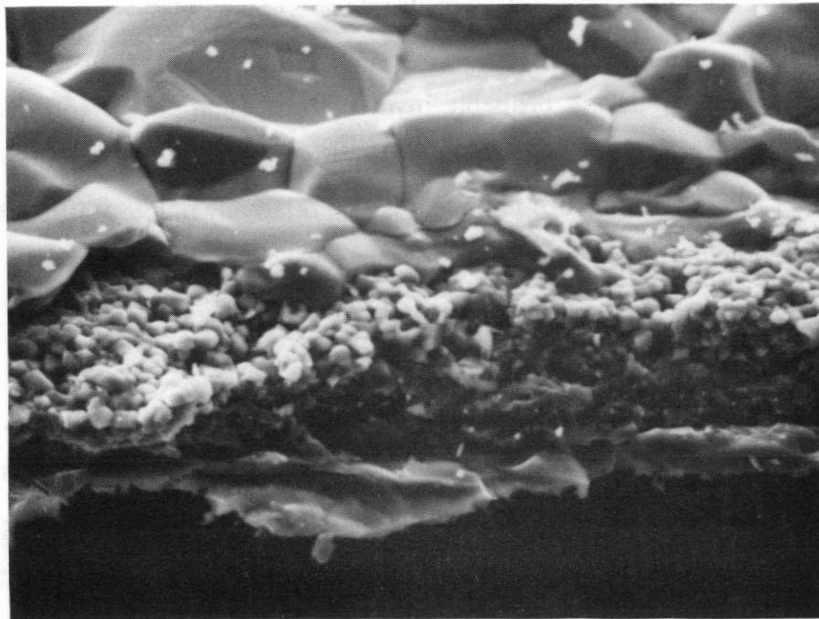
- (A): Rounded surface protrusion at outer portion of scale.
- (B): Outermost of the scale layers shown.
- (C): Central of the scale layers shown.
- (D): Innermost of the scale layers shown.
- (E): Subscale particles.



(a)

 $10\ \mu\text{m}$

M27759



(b)

 $10\ \mu\text{m}$

Fig. 22. Electron micrographs of the scale structure of specimen E1R8 after 24-h exposure in the "rich" sulfidizing atmosphere at 900°C: (a) Outer suite of scale layers, 55° tilt, and (b) inner suite of scale layers, 55° tilt.

Table 19. Qualitative EDS analyses for specimen E1R8 after 216-h exposure in the "rich" sulfidizing atmosphere at 900°C (summary of relative elemental abundance)^a

Chemical element	Feature in transverse section ^b		
	(A)	(B)	(C)
Iron	100	94	8
Chromium	7	100	100
Nickel	0	0.5	1
Manganese	16	16	3.7
Sulfur	0	2.7	39

^aRelative elemental abundance is in terms of each element's K- α excitation divided by that for the strongest element (presented as percentages).

^bKey to positions:

- (A): Large grains of the outermost scale layer.
- (B): Nodular grains in the central scale layer.
- (C): Featureless, lower layer in the outer scale layers.

It is seen that the outer two layers probably involve the formation of iron-rich compounds containing manganese and chromium; some of these compounds will later be shown to be spinels. The featureless inner layer is rich in chromium and is also relatively rich in sulfur. It is postulated that sulfur may have reached this position in the scale layer by means of the vein-like network, described earlier, which passes through the inner suite of scale layers; i.e., liquid sulfide transport through channels is proposed.

The SEM inspections and EDS analyses for the specimen exposed the shortest time, and in the "protective" region, indicated that the scales formed early in the process were also moderately complex. Low- and high-magnification electron micrographs for the specimen exposed for 2 h are presented in Fig. 23. Here, as shown in Fig. 23(a), the outer layer of the scale has partially spalled away, leaving behind a finer grain size inner scale layer adherent to the alloy substrate. The hemispherical protrusion seen standing upon the outer scale layer is believed to be similar to the cross section of the one shown in Fig. 20.

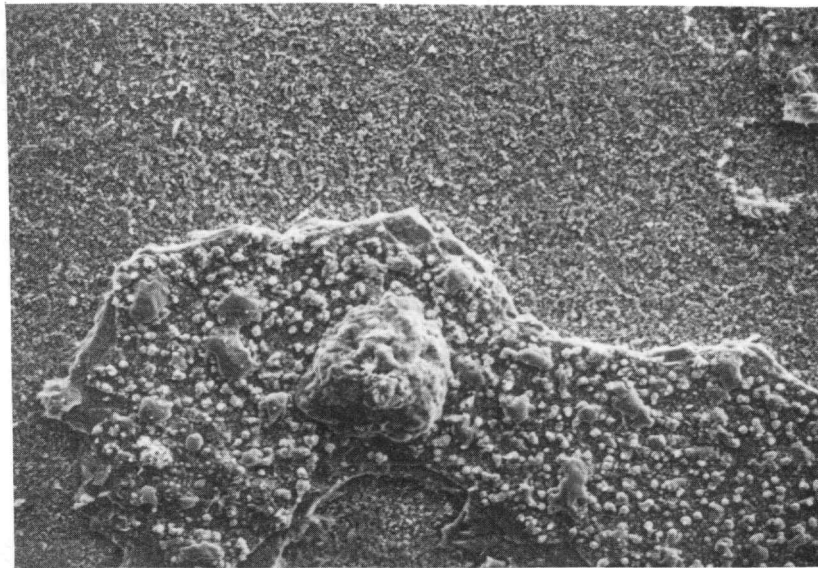
M27853



(a)

1.00 μm

M27850



(b)

100 μm

Fig. 23. Electron micrographs of the scale structure of specimen AR11 after 2-h exposure in the "rich" sulfidizing atmosphere at 900° C: (a) Overview of specimen; partially spalled specimen, and (b) bright Cr-S crystals; part of inner scale.

Selected results of the EDS analysis for this specimen are presented in Table 20. It is seen that both the inner and outer scale layers contain regions of considerable sulfur content. For the inner scale layer, sulfur was found to be concentrated in association with chromium at a relatively small number of bright hexagonal crystals, shown in Fig. 23(b). At the outer surface, sulfur is found in profusion associated with nickel in glassy nodules—obviously molten at the test temperature.

Table 20. Qualitative EDS analysis for specimen AR11 after 2-h exposure in the "rich" sulfidizing atmosphere at 900° (summary of relative elemental abundance)^a

Chemical element	Feature in plan section ^b			
	(A)	(B)	(C)	(D)
Iron	100	50	7.3	1.1
Chromium	52	100	12	76
Nickel	24	6	97	4
Manganese	4	4	6	1
Silicon	3	3	0	2
Sulfur	11	76	100	100

^aRelative elemental abundance is in terms of each element's K- α excitation divided by that for the strongest element (presented as percentages).

^bKey to positions:

- (A): Inner scale layer; integral chemistry.
- (B): Bright, hexagonal crystal on inner scale layer.
- (C): Glassy nodule on outer scale layer.
- (D): Sulfur-rich spalled particle (outer layer).

In an attempt to further analyze this extremely complex structure, the same specimen, with a portion of its outermost scale spalled away, was examined by X-ray diffraction; the findings are presented in Table 21. As is seen there, two austenite phases of slightly different lattice parameter were present. The dominant pattern is most probably associated either with alloy particles within the scale or with a separated layer of metal, as shown in Fig. 19. The strongest oxide patterns present are those associated with $Mn_{1.5}Cr_{1.5}O_4$ and Cr_2O_3 . Finally, weak patterns

Table 21. X-ray diffraction data for specimen AR11 after 24-h exposure in "lean" sulfidizing atmosphere at 900°C

Diffraction data [austenitic matrix (G ^γ)]			JCPDS card 33-397 (chromium iron nickel)		
Strong components					
2 θ	d (Å) ^a	I/I ₀ ^b	(hkl)	d (Å) ^a	I/I ₀ ^b
43.4677	2.0802	100	(111)	2.075	100
50.5566	1.8039	6	(200)	1.796	45
74.7546	1.2689	18	(220)	1.269	26
Not detected	-----	-----	(311)	1.082	30
96.189 ^c	1.0350	<2	(222)	1.037	12
Not detected	-----	-----	(400)	0.898	3
Diffraction data [spinel oxide scale (S1)]			JCPDS card 33-892 (Mn _{1.5} Cr _{1.5} O ₄)		
2 θ	d (Å) ^d	I/I ₀ ^e	(hkl)	d (Å) ^d	I/I ₀ ^e
18.1558	4.8822	13	(111)	4.88	25
29.7440	3.0012	52	(220)	2.985	50
35.0235	2.5600	100	(311)	2.545	100
36.6564	2.4496	7	(222)	2.438	6
42.5509	2.1229	11	(400)	2.110	20
52.7429	1.7342	11	(422)	1.723	10
56.2877	1.6331	11	(511)	1.625	30
62.6294	1.5037	35	(440)	1.493	45
Not detected	-----	-----	(533)	1.288	6
Not detected	-----	-----	(622)	1.273	2
Diffraction data [spinel oxide scale (S1)]			JCPDS card 33-892 (Mn _{1.5} Cr _{1.5} O ₄)		
2 θ	d (Å) ^f	I/I ₀ ^g	(hkl)	d (Å) ^f	I/I ₀ ^g
43.6692	2.0711	100	(111)	2.075	100
50.8966	1.7927	40	(200)	1.796	45
74.9038	1.2667	88	(220)	1.269	26
90.958	1.0804	30	(311)	1.082	30
96.283	1.0342	6	(222)	1.037	12
118.598	0.8959	6	(400)	0.898	3
Diffraction data (sesquioxide scale)			JCPDS card 6-504 (Cr ₂ O ₃)		
2 θ	d (Å) ^f	I/I ₀ ^h	(hkl)	d (Å) ^f	I/I ₀ ^h
24.5223	3.6272	69	(012)	3.633	75
33.5809	2.6666	100	(104)	2.666	100
36.1207	2.4847	44	(110)	2.480	95

Table 21. (Continued)

Diffraction data (sesquioxide scale)			JCPDS card 6-504 (Cr ₂ O ₃)		
39.829	2.2614	10	(006)	2.264	12
41.456	2.1764	25	(113)	2.176	40
Not detected	-----	-----	(202)	2.048	10
50.164	1.8171	28	(024)	1.816	40
54.730	1.6758	59	(116)	1.672	90
Not detected	-----	-----	(122)	1.579	14
63.257	1.4689	10	(214)	1.465	25
64.8530 ^j	1.4365	<20	(300)	1.431	40
72.7196 ^j	1.2993	<26	(10:10)	1.296	20
Not detected	-----	-----	(220)	1.240	18
Not detected	-----	-----	(306)	1.210	8
Not detected	-----	-----	(312)	1.173	14
Not detected	-----	-----	(02:10)	1.148	10
Not detected	-----	-----	(134)	1.124	10
Not detected	-----	-----	(226)	1.087	18
Not detected	-----	-----	(21:10)	1.042	16
Diffraction data (sulfide scale)			JCPDS card 2-1273 (NiS _{1.03})		

Weak Components

2 θ	d (Å) ^f	I/I ₀ ^g	(hkl)	d (Å) ^f	I/I ₀ ^g
30.0320	2.9731	89	(100)	2.98	60
Not detected	-----	-----	(002)	2.69	10
Sesquioxide interference			(101)	2.62	50
45.5030	1.9918	100	(102)	1.99	100
53.2846 ^k	1.7178	<33	(110)	1.72	80
Not detected	-----	-----	(103)	1.53	40
62.204 ^k	1.4912	<55	(200)	1.49	40
64.8530 ^j	1.4365	<51	(201)	1.44	40
Not detected	-----	-----	(004)	1.34	40
72.7196 ^j	1.2993	<67	(202)	1.30	70
Not detected	-----	-----	(104)	1.22	40
Not detected	-----	-----	(203)	1.14	20
Not detected	-----	-----	(210)	1.13	20
87.9812	1.1091	95	(211)	1.10	60
Not detected	-----	-----	(114)	1.06	70
96.1891 ^c	1.0350	<17	(212)	1.04	70
Not detected	-----	-----	(105)	1.01	20
103.336	0.9820	21	(300)	0.99	50
Not detected	-----	-----	(213)	0.95	40

Table 21. (Continued)

Diffraction data [spinel oxide scale (S2)]			JCPDS card 19-629 (Fe ₂ O ₃)		
2 θ	d (Å) ^l	I/I _o ^m	(hkl)	d (Å) ^l	I/I _o ^m
Not detected-----			(111)	4.852	8
30.1490	2.9618	43	(220)	2.967	30
35.3746	2.5354	86	(311)	2.532	100
Not detected-----			(222)	2.4243	8
43.0249	2.1006	52	(400)	2.0993	20
53.2846 ^k	1.7178	<37	(422)	1.7146	10
56.7778	1.6201	100	(511)	1.6158	30
62.204 ^k	1.4912	<62	(440)	1.4845	40
Not detected-----			(531)	1.4192	2
Not detected-----			(620)	1.3277	4
Not detected-----			(533)	1.2807	10
Austenite interference			(622)	1.2659	4
Not detected-----			(444)	1.2119	2
Not detected-----			(642)	1.1221	4
Not detected-----			(731)	1.0930	12
Not detected-----			(800)	1.0496	6
Not detected-----			(660)	0.9896	2
Not observed-----			(751)	0.9695	6

^aa_o = 3.59 Å; not (110) texture.

^bI_o = 9815 cpm. Probably represents metallic particles in the scale.

^cLine shared by austenite (G') and sulfide scale.

^da_o = 8.94 Å; strained and large grain size.

^eI_o = 8160 cpm; apparently not textured.

^fa_o = 3.586 Å; some (110) texture.

^gI_o = 5139 cpm; probably represents the substrate alloy.

^hI_o = 3540 cpm; evidence for some (104) texture.

ⁱLines shared by sesquioxide and sulfide scale.

^jI_o = 1411 cpm.

^kLines shared by sulfide scale and spinel oxide scale (S2).

^la_o ~ 8.41 Å; spinel is highly textured.

^mI_o = 1252 cpm.

are obtained for $\text{NiS}_{1.03}$ and Fe_3O_4 , the former possibly being weak because it occurs only in part as a crystalline phase and the latter being weak because most of this phase has spalled away from its site at the external surface.

Analyses by X-ray diffraction applied to specimens that had been exposed for times longer than 2 h revealed that other phases might also form in this environment. For such specimens, the additional structures found included those having the structural types of FeO , FeS , and MnFe_2O_4 , the latter two of these being homologous with other monosulfides and spinels, respectively.

4. DISCUSSION

In this section of the report, the findings of this experimental research program are discussed with respect to the observations and inferences drawn by others from either similar or allied studies.

4.1 THERMOCHEMICAL CONSIDERATIONS

The atmospheres utilized in this investigation, as well as their relation to both the usual thermodynamic parameters associated with the 310S material constituents and the coal gasification regime, are illustrated in the thermochemical diagram of Fig. 24. This diagram was constructed for the temperature of 900°C using thermochemical data for the lowest oxidation state and, therefore, the most stable oxides and sulfides of interest.⁸⁻¹¹ The range of oxygen and sulfur potentials representing the coal gasification regime, taken from Ref. 12, was then superimposed upon that diagram. Finally, the sulfur and oxygen potentials for the atmospheres used in this work are entered onto the diagram as the letters "A," "B," and "C," corresponding to their potentials as calculated for cases A, B, and C, respectively, in the Appendix.

It is seen that the test atmospheres used in this research surround, but do not intercept, those of the coal gasification regime. The tests conducted in air cannot be represented, as their sulfur potential is zero. The "lean" sulfidizing atmospheres start at relatively low sulfur pressures (*a*), and as the specimen reacts with the gaseous dissociation products of CaSO_4 , thereby consuming oxygen, the gas composition within the capsule is altered to one of higher sulfur pressure (*b*). For the case of the "rich" sulfidizing atmosphere, the gas composition within the capsule starts at point (*c*); however, its variation with the course of reaction has not been addressed here.

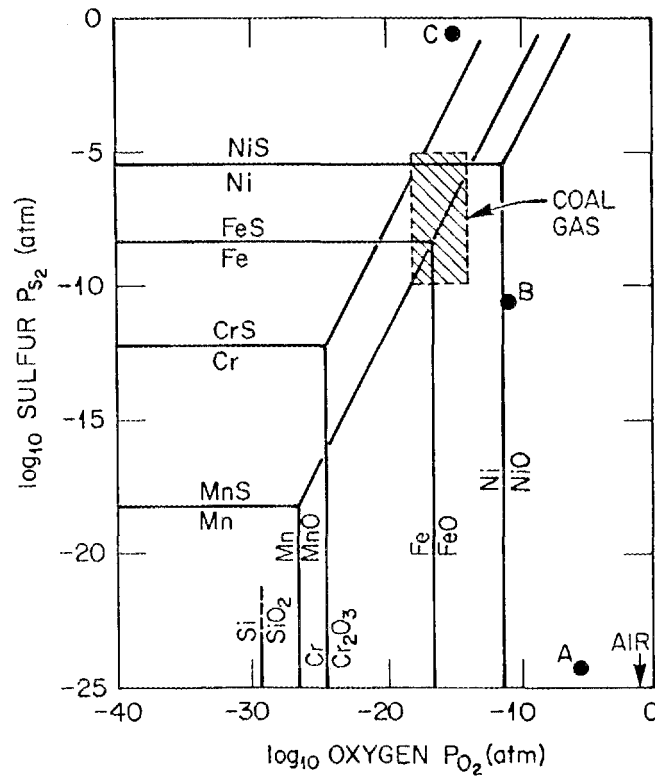


Fig. 24. Thermochemical diagram at 900°C for the constituents of 310S illustrating their critical oxygen and sulfur potentials, the atmospheres used in the research, and the gas potentials associated with the coal gasification regimen.

The diagram also illustrates that, from a thermodynamic point of view, the relative affinities of the constituent metals for oxygen and sulfur are essentially parallel; i.e., among them, manganese is most reactive and nickel is least reactive with either oxidant. The diagram is, of course, simplified in that it is constructed on the basis of pure elemental metals and reactants without consideration of their actual chemical activities in the 310S alloy. The thermodynamically predicted high reactivity of manganese has been reflected here in its ubiquitous presence in the oxidic reaction products; however, the extremely high mobility of manganese necessary for its kinetic participation in these reactions cannot be explained simply by this energetic consideration.

Another important aspect of thermochemical considerations, which bears upon the interpretation of the results of these experiments, is the potential for the formation of liquid phases, especially in those cases where the "rich" sulfidizing atmosphere has been employed. It is well known that the metal sulfides, as a class of materials, have lower melting points than their

inspected for their potential to liquify during the exposures used here. In Table 22 are presented the approximate melting points of the metal sulfides of interest to this system, as well as some selected eutectic temperatures for binary metal-metal sulfide systems.¹³

Table 22. Melting temperatures of selected metal sulfides and eutectic temperatures¹³

Sulfide or eutectic	Melting or eutectic point, °C
Melting monosulfides	
NiS	810
FeS	1195
MnS	1325
CrS	1550
TiS	2100
Binary eutectics	
Ni-Ni ₃ S ₂	645
Fe-FeS	985
Mn-MnS	1240

It is seen that nickel sulfide and its eutectic with nickel, if they form at the 900°C reaction temperature used in this work, will be liquid. There is, of course, the possibility of higher order sulfide eutectics, with correspondingly lower melting points, also forming as liquids with the test conditions used here. Good evidence has been presented above that, in the "rich" sulfidizing atmosphere, a nickel or similar sulfide did form as a liquid during reaction. While this sulfide was detected at the external surface of some scales and upon the upper portion of the inner suite of scale layers in others, its origin was most probably deep within the scaling system. This is so because the outermost scale layers are oxides and typically barren of nickel. Thus, the sulfide may have been extruded outward, through the vein network discussed in reference to Figs. 20 and 21, driven by the volumetric expansion of the forming nickel sulfide beneath the scale.

It is noted that, if one produces environments even more harsh than that associated with the "rich" atmosphere used here, then the corrosion process will become even more accelerated.

For example, by producing sulfur pressures near 10^{-7} atmosphere in the absence of oxygen, one may produce microstructures similar to that shown in Fig. 19 (900°C), in that internal sulfidation occurs at temperatures as low as 650°C in this steel.¹⁴

4.2 DEFORMATION CONSIDERATIONS

The deformations that we have observed in this work must necessarily have arisen from the generation of stresses that occurred either during the high-temperature exposures or during the transient heating or cooling operations. In the discussion which follows, it is presumed that the majority of the stress-related effects occurred at elevated temperatures.

The mechanisms for stress relaxation in oxides growing upon metallic substrates have been reviewed by Stringer¹⁵ and Kofstad.¹⁶ Among the isothermal stress-generating mechanisms that have been proposed are:

1. pre-oxidation and pre-treatment effects involving impurities or "inherited" stresses;
2. volumetric changes based upon the Pilling-Bedworth ratio;
3. scale or transformation reactions involving dilatation;
4. oxygen dissolution in metals, with lattice expansion;
5. compositional changes in the oxide or metal near their common interface;
6. epitaxial stresses involving the scale and its substrate;
7. oxide growth within the scale, including specifically grain-boundary oxidation;
8. vacancy injection into the metal; and
9. specimen geometry effects, especially with consideration of a coherent metal-scale interface (versus voids).

Among the isothermal stress-relaxation mechanisms that have been proposed are:

1. detachment of the scale near the metal-oxide interface, resulting in spalling;
2. elastic fracture or cracking of the scale layer;
3. recrystallation of the scale compounds;
4. plastic deformation and/or creep of the scale; and
5. deformation of the substrate metal or alloy.

A specialized mechanism involving vacancy injection coupled with interfacial dislocations has recently been proposed by Pieraggi and Rapp.¹⁷ It provides for the following features: (1) lateral compressive stresses in the scale layer, (2) lateral tensile stresses in the metallic

substrate, and (3) maintenance of the metal-scale interface in its natural recession during oxide growth. These macroscopic effects are similar in kind to those provided in an earlier model of oxide growth within the scale layer at grain boundaries.^{7,18} No firm conclusion may be drawn as to which of all the stress generation models is most correct; however, much of what has been observed in this work may be rationalized qualitatively on the basis of the Pieraggi-Rapp mechanism.

The application of this mechanism to type 310S steel is supported by our observation of a nominally coherent metal-oxide interface as shown in Fig. 7 and by void areas (condensed injected vacancies), especially on the alloy grain-boundary network as seen in Fig. 13(a). The linear dilatation of flat specimens in proportion to their degree of oxidation (Tables 4 and 13) and the earing of scale layers as shown in Fig. 19 are the types of deformation expected from the predicted stress state. The closure of "ells" depends upon the maintenance of the metal-oxide interface under the constraint that the retreating convex interface decreases in area, while that of the concave interface increases. Thus, to maintain both scale and interfacial continuities, the "ell" must necessarily close (Table 4) as the result of oxide formation by cation diffusion.

The lack of observed dilatation for specimens exposed to the "rich" sulfidizing atmosphere is consistent with their attendant liquid sulfide formation, as it is not possible to transmit large tractive forces across an interface containing liquid. It is the grossly different deformational behavior exhibited by the specimens exposed in air and those exposed in the "lean" sulfidizing environment that requires further explanation.

It was found that the deformation of specimens subjected to oxidation in air was very much larger than that observed when the specimens were exposed to the "lean" sulfidizing atmosphere. This occurred in spite of the fact that only oxides formed in both cases, and while a lesser amount of oxide was present in the "lean" sulfidizing environment, the deformations found there were less than they would have been had the deformation been proportional to the total amount of scale formation. It is believed that a primary cause of this apparently anomalous behavior is associated with phenomena that lead to the inclusion of metallic particles in the scale of the specimens exposed to the lean atmosphere (Fig. 17), an occurrence not seen in air. A second factor that may have diminished the deformation of these specimens is the fact that they do not, at least initially, form compact scales; rather, the open-bladed structures exemplified by Figs. 15 and 16 occur, and the generation of lateral stresses is, therefore, not expected in the outer reaches of these scales. Conversely, the scales formed in air are compact, and cooperative tractions may be large (as has been shown, for example, in Table 4 and Fig. 9). A further discussion of the "metal inclusion" effect will be presented below.

4.3 STRUCTURAL AND KINETIC CONSIDERATIONS

It is clear that the air-formed scales are bilayered in their nature, having a distorted sesquioxide proximal to the alloy, which is chemically similar to Cr_2O_3 and that exhibits some tendency for (110) texture. This scale layer is evidently highly stressed initially, as if by epitaxial forces, as its lattice parameters change during the initial few hours of its development. Upon this inner layer develops a spinel of an $(\text{Mn,Cr})_3\text{O}_4$ type, which initially has a very large lattice parameter (8.55 Å) that, at later times, undergoes a solid-state reaction to produce two spinels of lattice parameters 8.46 and 8.50 Å. It is suspected that such reaction is another possible evidence for stress alteration within the scale (generation or mitigation of stress depending upon detailed mechanism).

For those specimens oxidized in the "lean" sulfidizing atmosphere, the dominant crystal structures differ somewhat from those formed in air. The scale is again fundamentally bilayered; however, the underlying scale layer is a nearly undistorted form of Cr_2O_3 , stress relief perhaps having been achieved through the creation of the blade-like structures cited earlier. The overlying spinel scale layer, which apparently nucleates upon the inner layer, is of a generally smaller lattice parameter (8.45 Å) and corresponds closely to a compound of the type $\text{Mn}_{1.5}\text{Cr}_{1.5}\text{O}_4$. Thus, while similar in general type, the scale layers formed in air and those formed in the "lean" sulfidizing atmosphere exhibit some distinct topographic and structural differences, differences that are probably also reflected in the state of stress in these scales. Another investigator has found that the 310S alloy also exhibits the "spinel over Cr_2O_3 oxide" scale sequence in coal gasification atmospheres;¹⁹ however, the spinel cited is MnCr_2O_4 , a compound not currently listed in the JCPDS file. That investigator also has identified the oxide phase cited in the grain-boundary network of this alloy as a manganese-iron silicate, in very good agreement with the findings here regarding the filamentary network shown in Fig. 11(b).

This bilayered scale structure with the internal silicate (or silica) evidently remains stable for a relatively long time, the tests conducted here indicating low parabolic rates of thickening for times of up to approximately 400 h in the "lean" atmosphere. Indeed, a parallel behavior is exhibited by this alloy in high-BTU coal gasification atmospheres where the scale remains protective for up to 3,000 h before its breakdown occurs.¹⁹ That time of exposure, also at temperatures near 900°C, is approximately 10 times longer than the tests conducted in this work; unfortunately, it is also 3 to 10 times shorter than the target design life of certain coal gasifier components. Thus, the focus of future research must shift to the determination of why and how such breakdown occurs, in order that it may be prevented. The balance of this discussion will

focus upon those types of scales that are initially protective, as have been produced here by the "lean" atmosphere exposures and which appear to be closely related to those produced in actual coal gasification applications.

It has been found that, for scales formed on materials such as 310S to remain protective in actual application, the oxygen pressure in the gaseous phase must exceed approximately 10^3 times the equilibrium dissociation pressure of the protective chromia scale product.²⁰ This pragmatic limitation is recognized as a more qualitative statement of the fact that the activity of sulfur must not reach the critical value for compound nucleation in the region of the alloy-oxide interface, there being no simplistic relationship between that activity and the activity of gases at the gas-oxide interface.²¹ Thus, the problem of preventing scale breakdown in the long term must focus upon the quality of the protective oxide barrier with respect to sulfur transport, a kinetic consideration driven by the thermodynamic potentials involved and most probably modulated by the scale structure and/or its state of stress. For the case of iron-based alloys, relatively little is known regarding the relationship between scale microstructure and reaction kinetics.²² However, for alloys such as Fe-25Cr, it is believed that fine chromia grain sizes lead to faster rates of reaction.²³ This binary alloy probably reacts initially in a manner similar to the 310S steel. A relatively fine grain size was exhibited by the chromia scale layer developed in air on this steel, Fig. 8, which may also be representative of that formed in the "lean" sulfidizing atmosphere. Methods of developing coarser oxide grain sizes for the protective scale layer may, thus, be a fruitful area for future research.

While only trace amounts of sulfur were detected by EDS for the specimens exposed to the "lean" sulfidizing atmosphere, it is believed that sulfur does play a major role in the evolution of the scale microstructure, much the same as a catalyst might. It is well known that sulfur can permeate the protective oxide scales formed on many otherwise corrosion-resistant alloys, where it subsequently becomes associated with the alloy grain-boundary network and subsequently alters the initially formed scale layer.²⁴ Because, in alloys such as 310S, the depletion zone beneath the scale is relatively rich in nickel and poor in chromium (which is utilized in the initial scale formation), a condition is established that promotes nickel sulfide formation, finally leading to a breakaway reaction.²⁵ The presence of sulfur in the alloy grain boundaries was not confirmed in this work; however, the presence of nickel or an associated eutectic sulfide was established for the case of the rich sulfidizing environment.

It is believed that certain of the observations found in this work may be related to the ultimate breakdown of the protective layer. Thus, the metallic particles found embedded in the scale of the specimens oxidized in the "lean" sulfidizing atmosphere, Fig. 17, are believed to

represent the remnants of alloy grains which have been encapsulated as the scaling proceeds. As these embedded particles are absent in specimens exposed to sulfur-free air, it is postulated that they represent the remnants of alloy grains that have been encircled first by sulfide and later by oxide. This concept of particle formation infers that sulfur may have been transported through the oxide layers in sufficient quantity to react with the depleted alloy substrate along its grain boundaries.

As the particles are enriched in the less-reactive elements, iron and nickel, their continued reaction is limited so long as the oxide matrix in which they are embedded remains intact. However, should the oxide be disrupted in any manner, these particles would continue to oxidize in a state where they are thermally insulated from their substrate. As the heat of reaction cannot easily escape the region of the metallic particles, their temperature would ultimately rise (especially as they become smaller in dimension).²⁶ Given a large volume concentration of relatively small particles so trapped in the insulating layer, the local temperature may rise rapidly and thus lead to the breakdown of an otherwise protective scale.

The precise mechanism by which sulfur traverses the scale remains an open question. It has been shown that, for the case of an Fe-25Cr alloy at 900° C, the sulfur is associated with the grain-boundary network of the chromia scale and, incidentally, may decrease its rate of growth.²⁷ If chromia thickens by the transport of the cations through grain-boundary short-circuit paths, sulfur could serve as a temporary blocking agent enhancing the barrier quality of the scale. Ultimately, however, the sulfur will proceed to the alloy-oxide interface, and the protective nature of the barrier will be lost. For the case of unalloyed iron, which had been completely oxidized and subsequently exposed to a sulfur-bearing gas, it was found that the sulfur was associated only with the grain-boundary network of the scale and that it had completely penetrated the oxide body in a matter of minutes at 900° C.²⁸ While the oxide present was different in kind from that formed on 310S, this observation is important in that it may indicate a general tendency for the transport of sulfur via oxide grain boundaries. Other mechanisms for the transport of sulfur through scale layers have been considered and included: its dissolution in the oxide phase followed by diffusive transport and its transport as a sulfur-bearing gaseous phase via undefined physical discontinuities in the scale.²⁹ Obviously, further work will be required to first define the effective transport paths of sulfur and, second, to employ countermeasures for eliminating such paths in scales formed on engineering alloys in sulfidizing applications.

5. FUTURE WORK

As is evident from the above discussion, work is needed in the area of potential methods for obviating the breakaway phenomenon in alloys of technical interest. One type of research that seems particularly fruitful is the certain identification of the mechanism by which sulfur traverses the scale layer. It is our opinion that the path of primary concern involves the grain-boundary network of the scale and, therefore, it is suggested that this portion of the overall problem be addressed.

One method of securing this fundamental information involves using the "lean" sulfidizing atmosphere tests as described herein but with the late addition to the gaseous atmosphere of a sulfur species that differs in its isotopic distribution from that found in nature. The scales developed in such tests may then be analyzed using high-resolution secondary ion mass spectroscopy (SIMS) techniques to determine the precise sites at which sulfur is incorporated in the scale and at what stage in the evolution of scale development such incorporation occurs. This testing mode had been planned earlier but was not implemented during this reporting period due to time constraints. For these later specialized tests, a small lot of CaSO_4 containing 55.99% of the stable isotope sulfur-34 was secured through the Isotope Distribution Center at Oak Ridge National Laboratory. This material was prepared by the Stable Isotope Enrichment Department from a special lot of sulfur and has the isotopic abundances indicated in Table 23.

Table 23. Relative sulfur abundance in special CaSO_4 lot

Isotope	Analysis of CaSO_4	Natural abundance ³⁰
Sulfur-32	43.57%	95.02
Sulfur-33	0.42%	0.74
Sulfur-34	55.99%	4.22
Sulfur-36	<0.05%	0.02

It is hoped that, at some time in the future, the potentially informative research program utilizing this material may be initiated.

6. CONCLUSIONS

Sheet specimens of type 310S stainless steel of known dimension and form were exposed to air, a "lean" and a "rich" sulfidizing atmosphere, at temperatures near 900°C. Based upon the analyses of these specimens by various techniques, the following conclusions are drawn:

1. The scales formed in air and the "lean" atmosphere are protective and non-spalling while those formed in the "rich" atmosphere spall, react at rates 1,000 times greater in their quasi-protective mode, and later exhibit a "breakaway" reaction.

2. Only those scales formed in air provide the cooperative, tractive, interfacial forces required to produce uniform dilatation and deformation of the substrate.

3. Evidence is presented that the scales formed in air or in the sulfidizing atmospheres at 900°C are highly stressed. While the stresses in air-formed scales may be long range, those formed in sulfur-bearing atmospheres may be localized.

4. The scales produced on specimens exposed to the "lean" sulfidizing environment appear to mock those produced in actual coal gasification applications.

5. Two-layer scales are formed both in air and in the "lean" atmosphere, the inner layer being a sesquioxide and the outer layer being a spinel. However, the structural details of the scales formed in these two atmospheres are grossly different.

6. The metallic particles found embedded in the scale layers of those specimens exposed to the "lean" sulfidizing atmosphere may be indicative of a stage in scale evolution that is a precursor to the breakdown process of the protective scale.

7. Scales formed in the "rich" atmosphere are very complex, having a minimum of six scale layers and subscale product formation. Liquid sulfides are present at temperature and may permeate the inner suite of layers via their vein-like network.

8. Alloys containing high concentrations of nickel, such as 310S, are contraindicated for sulfidation applications due to their potential to form disruptive liquid sulfides at relatively low temperatures.

9. The control of protective oxide grain size may prove to be a fruitful approach in the future development of sulfidation-resistant alloys.

10. The testing method employing the "rich" sulfidizing atmosphere may be one that can be employed as an inexpensive and rapid screening method for determining the sulfidation resistance of new alloys as they are developed.

7. ACKNOWLEDGMENTS

This report results primarily from the 1987-1988 sabbatical research opportunity afforded one of the authors. It could not have been completed without the assistance of, and interaction with, many of the personnel of the Metals and Ceramics (M&C) Division. For their assistance in facilitating this work administratively, the authors thank V. J. Tennery, G. M. Slaughter, J. R. DiStefano, and K. Newport. For his helpful technical discussions in the area of sulfidation, the authors thank J. V. Cathcart. For their assistance in analytical and support services, the authors thank R. S. Crouse, B. C. Leslie, G. C. Marsh, J. W. Nave, and T. A. Nolan. For their assistance in the fabrication and exposure of specimens for this research, the authors thank J. J. Campbell, M. Howell, and E. J. Lawrence.

8. REFERENCES

1. P. H. Ableson, "Energy Futures," *Am. Sci.* **75**, 584-93 (1987).
2. H. S. Hsu, *A Review of the Development and Breakdown of Protective Oxide Scales on Alloys Exposed to Coal-Derived Atmospheres*, ORNL-6323, Martin Marietta Energy Systems, Inc., Oak Ridge National Lab., 1986.
3. N. Birks, G. H. Meier, and F. S. Pettit, "High-Temperature Corrosion Resistance," *J. Met.* **39**, 28-31 (1987).
4. R. H. Kane, "Alloy Selection for High-Temperature Corrosives," *Process Industries Corrosion*, ed. B. J. Moniz and W. I. Pollock, National Association of Corrosion Engineers, Houston, 1986.
5. *ASM Metals Reference Book*, 2nd ed., American Society for Metals, Materials Park, Ohio, 1983.
6. Oak Ridge National Laboratory, Analytical Chemistry Division, Analysis No. 880125-111, 1988.
7. J. S. Wolf, "An Investigation of the Effect of Specimen Geometry on the Oxidation of Nickel at Elevated Temperatures," Ph.D. thesis, University of Florida, 1965.
8. K. K. Kelly, "Contributions to the Data on Theoretical Metallurgy," Vol. VII, *The Thermodynamic Properties of Sulfur and its Inorganic Compounds*, Bureau of Mines, Bull. 406, 1937.

9. J. P. Coughlin, "Contributions to the Data on Theoretical Metallurgy," Vol. XII, *Heats and Free Energies of Formation of Inorganic Oxides*, Bureau of Mines, Bull. 542, 1954.
10. S. R. Shatynski, "The Thermochemistry of Transition Metal Sulfides," *Oxid. Met.* **11**, 307-20 (1977).
11. F. Gesmundo, C. De Asmundis, and C. Bottino, "High-Temperature Corrosion of Manganese in Pure SO₂," *Oxid. Met.* **14**, 15-29 (1980).
12. T. C. Tiarney and K. Natesan, "Metallic Corrosion in Simulated Low-Btu Coal-Gasification Atmospheres," *J. Mater. Energy Syst.* **1**, 13-29 (1980).
13. S. Mrowec and K. Przybylski, "Defect and Transport Properties of Sulfides and Sulfidation of Metals," *High Temp. Mater. Processes* **6**, 1-79 (1984).
14. P. I. Williams, R. G. Faulkner, L. W. Pinder, and D. J. Lees, "The Influence of Alloy Diffusion Processes on the Corrosion of Ferritic and Austenitic Stainless Steels," *Corros. Sci.* **27**, 595-613 (1987).
15. J. Stringer, "Stress Generation and Relief in Growing Oxide Films," *Corros. Sci.* **10**, 513-43 (1970).
16. P. Kofstad, *High Temperature Corrosion*, Elsevier Applied Science, New York, 1988.
17. B. Pieraggi and R. A. Rapp, "Stress Generation and Vacancy Annihilation During Scale Growth Limited by Cation-Vacancy Diffusion," *Acta. Metall.* **36**, 1281-89 (1988).
18. F. N. Rhines and J. S. Wolf, "The Role of Oxide Microstructure and Growth Stresses in the High-Temperature Scaling of Nickel," *Metall. Trans.* **1**, 1701-10 (1970).
19. R. A. Perkins, "Development of Alloys for Use in Coal Derived Gases," pp. 345-53 in *High Temperature Corrosion*, NACE-6, National Association of Corrosion Engineers, Houston, 1983.
20. K. Natesan, "High-Temperature Corrosion in Coal Gasification Systems," *Corrosion* **41**, 646-55 (1985).
21. F. S. Pettit, J. A. Goebel, and G. W. Goward, "Thermodynamic Analysis of the Simultaneous Attack of Some Metals and Alloys by Two Oxidants," *Corros. Sci.* **9**, 903-13 (1969).
22. K. Ishiguro and T. Homma, "Thin Oxide Films on a Ferritic and an Austenitic Alloy," pp. 28-34 in *High Temperature Corrosion*, NACE-6, National Association of Corrosion Engineers, Houston, 1983.
23. M. J. Graham, "Thin Oxide Film Formation on Metals," pp. 139-44 in *High Temperature Corrosion*, NACE-6, National Association of Corrosion Engineers, Houston, 1983.

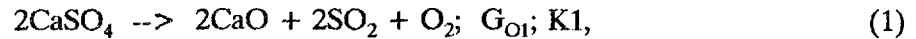
24. J. Stringer, A. J. Minchener, D. M. Lloyd, and H. R. Hoy, "In-Bed Corrosion of Alloys in Atmospheric Fluidized Bed Combustors," pp. 433-47 in *Proceedings of the Sixth International Conference on Fluidized Bed Combustion*, Vol. 2, U.S. DOE, 1980.
25. R. C. Lobb and H. E. Evans, "Observations on the Effect of Low Sulfur Activity on the Oxidation of Chromium-Depleted Zones in a Stainless Steel," *Oxid. Met.* **15**, 371-84 (1981).
26. J. S. Wolf, *Exploratory Development on Oxidation Behavior of Titanium Alloys under High Heating Rates*, AFML-TR-74-265, April 1975.
27. Y. K. Kim, K. Przyblski, and G. J. Yurek, "Segregation of Sulfur to Grain Boundaries in Chromia and Alumina Scales," pp. 259-81 in *Fundamental Aspects of High Temperature Corrosion II*, Electrochemical Society, Pennington, N.J., 1986.
28. F. C. Yang and D. P. Whittle, "Sulfur Diffusion in Oxide Grain Boundaries," *Corros. Sci.* **23**, 285-90 (1983).
29. P. Singh and N. Birks, "Penetration of Sulfur through Preformed Protective Oxide Scales," *Oxid. Met.* **19**, 37-52 (1983).
30. D. E. Gray, ed., *American Institute of Physics Handbook*, 3rd ed., McGraw-Hill, New York, 1972.

APPENDIX

**GAS PRESSURE ESTIMATES FOR CAPSULE TESTS INVOLVING THE
DISSOCIATION OF CALCIUM SULFATE WITH AND WITHOUT
ELEMENTAL SULFUR PRESENT**

The purpose of this Appendix is to describe an approach used to calculate the gas pressures generated in evacuated and sealed capsules containing one or two gas-producing reagents. The reagents considered are: (1) anhydrous calcium sulfate alone and (2) anhydrous calcium sulfate in combination with elemental sulfur. The particular situation(s) being modeled are those wherein the reagent(s) and a metallic specimen are within an evacuated quartz capsule, which is subsequently to be heated to some constant temperature. It is assumed that: (1) there is no physical contact between the reagent(s) and the metal and (2) the activities of all condensed phases are unity.

The gases evolved from the heating of calcium sulfate involve two dissociation reactions, which are sequential:



and



For those cases where solid sulfur is present in the initial capsule charge, gaseous sulfur will be produced by the single reaction:



Two types of cases will be discussed here, one being for the situation where the metallic specimen is absent or non-reactive and the second for the case where the specimen reacts with the gaseous dissociation products.

Case A. Non-Reactive System (large CaSO₄ supply; no sulfur)

For this case, the dissociations will eventually lead to the production of equilibrium gas pressures. As the temperature dependence of (G_{O1}) and, therefore, ($K1$) are known, the equilibrium constant may be expressed as:

$$K1 = (P_{O2})(P_{SO2})^2 = 4(P_{O2})^3 = \exp(-G_{O1}/RT), \quad (4)$$

from which first (P_{O_2}) and subsequently (P_{SO_2}) may be determined as, for this step, the value of (P_{SO_2}) is twice that of (P_{O_2}).

Some small fraction (f) of that initially formed SO_2 dissociates in accordance with the second reaction to produce: sulfur vapor at a pressure of $f^*(P_{SO_2})$ and oxygen gas at a pressure of $2f^*(P_{SO_2})$. As the temperature dependence of (G_{O_2}) and (K_2) are also known, the equilibrium constant may be written as:

$$K_2 = (P_{S_2})(P_{O_2})^2/(P_{SO_2})^2 = 4(f^3)(P_{SO_2}), \quad (5)$$

from which the value of (f) may be calculated, as (P_{SO_2}) is essentially invariant during the second dissociation step, values of (f) typically being less than 10^{-6} for temperatures at or below $1000^\circ C$.

Applying this approach, the relevant equilibrium gas pressures at $900^\circ C$ are found to be:

$$\begin{aligned} (P_{SO_2}) &= 3.40 \times 10^{-6} \text{ atm,} \\ (P_{O_2}) &= 1.70 \times 10^{-6} \text{ atm, and} \\ (P_{S_2}) &= 5.00 \times 10^{-25} \text{ atm.} \end{aligned} \quad (6)$$

It is seen that the primary dissociation controls the pressures of SO_2 and O_2 , while the secondary dissociation controls the pressure of S_2 for this case. This is so because the second dissociation fraction (f) is of very small magnitude.

Case B. Reactive System

For the case of a reactive system, the behavior of the gas pressures with time is obviously governed primarily by kinetic considerations. This situation is addressed in two stages, the first dealing with thermodynamic limits for systems in equilibrium and the second dealing with a method of estimating the gas pressures for a dynamic system.

Case B1. Equilibrium Considerations

We have shown above that the inner scale layer formed on type 310S stainless steel, in either air or the lean sulfidizing atmosphere, is essentially Cr_2O_3 and that chromium sulfides are not evident. One limiting circumstance may be described by setting the oxygen pressure equal to that dictated by the equilibrium between chromium metal (representing the 310S alloy) and oxygen. That pressure at a temperature of $900^\circ C$ is illustrated in Fig. 24 of the main text. Applying this approach, the relevant equilibrium gas pressures at this temperature may be calculated from the known values of the equilibrium constants. Those pressures are found to be:

$$\begin{aligned}
 (P_{\text{SO}_2}) &= 9.85 \times 10^{+3} \text{ atm,} \\
 (P_{\text{O}_2}) &= 2.03 \times 10^{-25} \text{ atm, and} \\
 (P_{\text{S}_2}) &= 9.85 \times 10^{+32} \text{ atm.}
 \end{aligned}
 \tag{7}$$

This limiting set of pressures is not realistic with respect to the capsule tests that the authors have conducted; however, they do illustrate the dramatic increases in the sulfidizing gas pressures due to decreasing the oxygen pressure.

A second limiting circumstance may be described by examining the equilibrium resulting from the intimate contact of calcium sulfate with the chromium metal. In this instance, the oxygen and sulfur pressures (activities) are set equal to those dictated by the equilibria between chromium metal, oxygen, and sulfur as illustrated in Fig. 24 of the main text. Applying the same approach as was used above, the effective equilibrium pressure of SO_2 may also be calculated. Those pressures at a temperature of 900°C are:

$$\begin{aligned}
 (P_{\text{SO}_2}) &= 4.66 \times 10^{-19} \text{ atm,} \\
 (P_{\text{O}_2}) &= 2.03 \times 10^{-25} \text{ atm, and} \\
 (P_{\text{S}_2}) &= 6.62 \times 10^{-23} \text{ atm.}
 \end{aligned}
 \tag{8}$$

While the sulfidizing gas pressures are considerably smaller than those of the previous example, this limiting set of pressures is also not realistic with respect to the capsule tests that the authors have conducted. Rather, they represent the expected activities at the interface between chromium metal and a coherent overlayer of CaSO_4 .

What are desired are the pressures of the species in the gas phase, which is addressed next.

Case B2. Kinetic Considerations (large CaSO_4 supply)

For this case, the dissociations will eventually lead to the production of steady-state gas pressures. In order to carry out the estimation of these gas pressures, under the condition that the specimen is fixing only the oxygen, one must assume that the dissociations occur at infinite velocity.

As with case A, the first dissociation produces both SO_2 and O_2 ; however, the O_2 is consumed rapidly by the specimen as (P_{O_2}) is greater than the dissociation pressure of the metal oxide being formed. As a consequence of this pumping action, the value of (P_{SO_2}) must rise in order to maintain the equilibrium constant for the first reaction at a fixed value; as:

$$K_1 = (P_{\text{O}_2})(P_{\text{SO}_2})^2. \tag{9}$$

However, the rising pressure of SO₂ must necessarily cause the values of both (P_{O₂}) and (P_{S₂}) to increase in order to maintain the value of the equilibrium constant for the second reaction fixed as:

$$K_2 = (P_{S_2})(P_{O_2})^2/(P_{SO_2})^2. \quad (10)$$

These pressure increases do not proceed without limit for two reasons. Firstly, as (P_{SO₂}) increases, its degree of dissociation must decrease in accordance with:

$$K_2 = 4(f^3)(P_{SO_2}) \text{ or } f = (K_2/4)^{(1/3)} (P_{SO_2})^{(-1/3)}, \quad (11)$$

and, secondly, the value of (K₁) must remain constant. It follows that:

$$(P_{O_2})(P_{SO_2})^2 = K_1 \quad (12)$$

from the first dissociation, and

$$(P_{O_2}) = 2[(K_2/4)^{(1/3)}](P_{SO_2})^{(2/3)}. \quad (13)$$

from the second.

Upon substitution of the second of these equations into the first, one obtains the following value for the steady-state pressure:

$$(P_{SO_2}) = [K_1/(2K_2)^{(1/3)}]^{(3/8)}. \quad (14)$$

Applying this approach, the relevant equilibrium gas pressures at 900°C are found to be:

$$\begin{aligned} (P_{SO_2}) &= 5.93 \times 10^{-4} \text{ atm,} \\ (P_{O_2}) &= 5.60 \times 10^{-11} \text{ atm, and} \\ (P_{S_2}) &= 2.80 \times 10^{-11} \text{ atm.} \end{aligned} \quad (15)$$

It is seen that the secondary dissociation (K₂) now controls the pressures of O₂ and S₂, while the primary dissociation (K₁) controls the pressure of SO₂ for this case. The estimation method used here is believed to provide a realistic set of gas pressures for the case of the "lean" sulfidizing atmosphere as used in these tests.

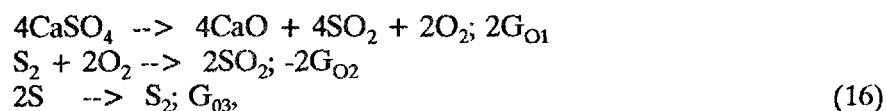
Added note: The results provided by this method of estimation may also be approximated by means of a "mental experiment" in which: (1) the gas pressures of case A are present at temperature in the closed capsule, (2) the metallic specimen is inserted and allowed to consume

some percentage of the oxygen present, (3) the metallic specimen is withdrawn and pressures are recalculated, and (4) the insertion-consumption-withdrawal processes are repeated. The gas pressures calculated by this iterative technique converge toward those cited above.

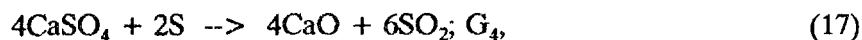
Case C. Non-Reactive System (large CaSO₄ and sulfur supplies)

This case addresses only that particular situation wherein the reagents are admixed in stoichiometric proportions with respect to the production of SO₂; i.e., the case where the mass of CaSO₄ in the charge is approximately 8.5 times that of sulfur. For the non-reacting system, the sulfur pressure is essentially predetermined by three system parameters: the mass of sulfur in the charge, the temperature of the capsule, and the volume of the capsule (42 ml).

The pressure of SO₂ may be determined by first summing the following reactions:



to give



and then solving the equilibrium relation:

$$P_{\text{SO}_2} = \exp(-G_4/6RT). \quad (18)$$

The oxygen pressure in this case will be that calculated from the equilibrium dissociations of SO₂ and CaSO₄ for those temperatures in the range of interest.

Applying this approach, the relevant equilibrium gas pressures at 900°C are found to be:

$$\begin{aligned} (P_{\text{SO}_2}) &= 7.40 \times 10^{-2} \text{ atm,} \\ (P_{\text{O}_2}) &= 3.60 \times 10^{-15} \text{ atm, and} \\ (P_{\text{S}_2}) &= 3.57 \times 10^{-1} \text{ atm.} \end{aligned} \quad (19)$$

It is seen that the addition of elemental sulfur strongly enhances the sulfur pressure, while decreasing the oxygen pressure, as compared to the cases where CaSO₄ is the lone reagent. The pumping action of a reactive specimen will not sensibly alter this situation, so long as the supply of reagents is large.

For the three cases discussed above, it is emphasized that: (1) the $\text{SO}_2\text{-SO}_3$ equilibrium has been neglected and (2) kinetic effects have, in no way, been taken into account. For a more complete discussion of equilibria in metal-oxygen-sulfur systems, the reader is referred to the work of others.*

*P. Sarrazin and A. Skalli, "Corrosion of Metals in Multicomponent Gas Atmospheres: Generalization of the Use of Phase-Stability Diagrams," *Oxid. Met.* **30**, 107-24 (1988).

INTERNAL DISTRIBUTION

- | | | | |
|--------|-------------------------------|--------|------------------------------|
| 1-2. | Central Research Library | 28. | R. C. Martin |
| 3. | Document Reference Section | 29. | H. E. McCoy |
| 4-5. | Laboratory Records Department | 30. | B. F. Myers |
| 6. | Laboratory Records, ORNL-RC | 31. | G. M. Slaughter |
| 7. | ORNL Patent Section | 32. | R. A. Strehlow |
| 8-10. | M&C Records Office | 33. | V. J. Tennery |
| 11. | R. A. Bradley | 34. | P. F. Tortorelli |
| 12. | P. T. Carlson | 35. | D. F. Wilson |
| 13-17. | O. B. Cavin | 36-40. | J. S. Wolf |
| 18. | D. F. Craig | 41. | Y. A. Chang (Consultant) |
| 19-23. | J. H. DeVan | 42. | H. W. Foglesong (Consultant) |
| 24. | E. L. Fuller | 43. | J. J. Hren (Consultant) |
| 25. | C. R. Hubbard | 44. | M. L. Savitz (Consultant) |
| 26. | R. R. Judkins | 45. | J. G. Simon (Consultant) |
| 27. | J. R. Keiser | 46. | K. E. Spear (Consultant) |

EXTERNAL DISTRIBUTION

- 47-48. AIR PRODUCTS AND CHEMICALS, P. O. Box 538, Allentown,
PA 18105
S. W. Dean
S. C. Weiner
49. ALBERTA RESEARCH COUNCIL, Oil Sands Research Department,
P.O. Box 8330, Postal Station F, Edmonton, Alberta,
Canada T6H5X2
L. G. S. Gray
- 50-51. ALLISON GAS TURBINE DIVISION, P.O. Box 420, Indianapolis,
IN 46206-0420
P. Khandelwal (Speed Code W-5)
R. A. Wenglarz (Speed Code W-16)
52. ARGONNE NATIONAL LABORATORY, 9700 S. Cass Avenue, Argonne,
IL 60439
K. Natesan

53. ARGONNE NATIONAL LABORATORY-WEST, P.O. Box 2528, Idaho Falls,
ID 83403-2528
S. P. Henslee
54. AVCO RESEARCH LABORATORY, 2385 Revere Beach Parkway, Everett,
MA 02149
R. J. Pollina
- 55-56. BABCOCK & WILCOX, 1562 Beeson Street, Alliance, OH 44601
T. I. Johnson
T. Modrak
57. BABCOCK & WILCOX, Domestic Fossil Operations,
20 South Van Buren Avenue, Barberton, OH 44023
M. Gold
58. BABCOCK & WILCOX, Lynchburg Research Center, P.O. Box 11165,
Lynchburg, VA 24506
H. Moeller
59. BATTELLE-COLUMBUS LABORATORIES, 505 King Avenue, Columbus,
OH 43201
I. G. Wright
- 60-62. BRITISH COAL CORPORATION, Coal Research Establishment, Stoke
Orchard, Cheltenham, Gloucester, England, GL52 4RZ
M. Arnold
C. Bower
A. Twigg
63. BRITISH GAS CORPORATION, Westfield Development Centre, Cardenden,
Fife, Scotland KY50HP
J. E. Scott
64. BROOKHAVEN NATIONAL LABORATORY, Department of Applied
Science, Upton, Long Island, NY 11973
T. E. O'Hare
- 65-66. CANADA CENTER FOR MINERAL & ENERGY TECHNOLOGY, 568
Booth Street, Ottawa, Ontario, Canada K1A 0G1
R. W. Revie
M. Sahoo

67. COMBUSTION ENGINEERING, 1000 Prospect Hill Road, Windsor,
CT 06095
D. A. Canonico
68. CONSOLIDATION COAL COMPANY, 4000 Brownsville Road, Library,
PA 15129
S. Harding
- 69-71. ELECTRIC POWER RESEARCH INSTITUTE, P.O. Box 10412, 3412
Hillview Avenue, Palo Alto, CA 94303
W. T. Bakker
J. Stringer
R. H. Wolk
72. EUROPEAN COMMUNITIES JOINT RESEARCH CENTRE, Petten
Establishment, P.O. Box 2, 1755 ZG Petten, The Netherlands
M. Van de Voorde
73. FLUIDIZED BED TECHNOLOGIES, P.O. Box 4469, Chattanooga,
TN 37405
R. Q. Vincent
74. FOSTER WHEELER DEVELOPMENT CORPORATION, Materials
Technology Department, John Blizard Research Center,
12 Peach Tree Hill Road, Livingston, NJ 07039
J. L. Blough
75. GAS RESEARCH INSTITUTE, 8600 West Bryn Mawr Avenue, Chicago,
IL 60631
H. S. Meyer
76. GENERAL ELECTRIC COMPANY, 1 River Road, Bldg. 55, Room 115,
Schenectady, NY 12345
R. W. Haskell
77. IDAHO NATIONAL ENGINEERING LABORATORY, P.O. Box 1625,
Idaho Falls, ID 83415
D. W. Keefer
78. IOWA STATE UNIVERSITY, Materials Science and Engineering Department,
110 Engineering Annex, Ames, IA 50001
K. M. Vedula

79. LAWRENCE BERKELEY LABORATORY, University of California, Berkeley,
CA 94720
A. V. Levy
80. LAWRENCE LIVERMORE LABORATORY, P.O. Box 808, L-325, Livermore,
CA 94550
W. A. Steele
81. MOBIL RESEARCH & DEVELOPMENT CORPORATION,
P.O. Box 1026, Princeton, NJ 08540
R. C. Searles
82. NATIONAL MATERIALS ADVISORY BOARD, National Research Council,
2101 Constitution Avenue, Washington, DC 20418
K. M. Zwilsky
- 83-84. NEW ENERGY AND INDUSTRIAL TECHNOLOGY DEVELOPMENT
ORGANIZATION, Sunshine 60 Bldg., P.O. Box 1151, 1-1, Higashi-
Ikebukuro 3-chrome, Toshima-Ku, Tokyo, 170, Japan
H. Narita
S. Ueda
85. RISOE NATIONAL LABORATORY, P.O. Box 49, DK-4000, Roskilde,
Denmark
A. Olsen
86. SHELL DEVELOPMENT COMPANY, P.O. Box 1380, Houston,
TX 77251-1380
L. W. R. Dicks
87. SOUTHWEST RESEARCH INSTITUTE, 6620 Culebra Road,
P.O. Drawer 28510, San Antonio, TX 78284
F. F. Lyle, Jr.
- 88-89. TENNESSEE VALLEY AUTHORITY, 1101 Market Street,
Missionary Ridge, Chattanooga, TN 37402-2801
C. M. Huang
A. M. Manaker
90. TEXAS EASTERN TRANSMISSION CORPORATION, P.O. Box 2521,
Houston, TX 77252
D. H. France

91. THE MATERIALS PROPERTIES COUNCIL, INC., United Engineering Center, 345 E. Forty-Seventh Street, New York, NY 10017
M. Prager
92. THE TORRINGTON COMPANY, Advanced Technology Center, 59 Field Street, Torrington, CT 06790
W. J. Chmura
93. UNIVERSAL ENERGY SYSTEMS, INC., 4401 Dayton-Zenia Road, Dayton, OH 45432
V. Srinivasan
- 94-95. UNIVERSITY OF CALIFORNIA AT BERKELEY, Berkeley, CA 94720
J. A. C. Humphrey, Dept. of Mechanical Engineering
E. R. Parker, Dept. of Materials Science and Mineral Engineering
96. UNIVERSITY OF TENNESSEE AT KNOXVILLE, Materials Science and Engineering Department, Knoxville, TN 37996
C. D. Lundin
97. UNIVERSITY OF TENNESSEE SPACE INSTITUTE, Tullahoma, TN 37388
J. W. Muehlhauser
98. WESTERN RESEARCH INSTITUTE, 365 N. 9th Street, P.O. Box 3395, University Station, Laramie, WY 82071
V. K. Sethi
99. WESTINGHOUSE ELECTRIC CORPORATION, Research and Development Center, 1310 Beulah Road, Pittsburgh, PA 15235
S. C. Singhal
100. WESTINGHOUSE HANFORD COMPANY, P.O. Box 1970, W/A-65, Richland, WA 99352
R. N. Johnson
101. DOE, OFFICE OF BASIC ENERGY SCIENCES, Materials Science Division, ER-131, GTN, Washington, DC 20545
J. B. Darby
102. DOE, OFFICE OF CONSERVATION AND RENEWABLE ENERGY, CE-12, Forrestal Building, Washington, DC 20545
J. J. Eberhardt

- 103-110. DOE, MORGANTOWN ENERGY TECHNOLOGY CENTER, P.O. Box 880,
Morgantown, WV 26505
R. A. Bajura
R. C. Bedick
D. C. Cicero
F. W. Crouse, Jr.
N. T. Holcombe
W. J. Huber
J. E. Notestein
J. S. Wilson
111. DOE, OFFICE OF FOSSIL ENERGY, Washington, DC 20585
J. P. Carr, FE-14
112. DOE, PITTSBURGH ENERGY TECHNOLOGY CENTER, P.O. Box 10940,
Pittsburgh, PA 15236
A. H. Baldwin
G. V. McGurl
R. Santore
T. M. Torkos
- 113-114. DOE OAK RIDGE FIELD OFFICE, P.O. Box 2008, Oak Ridge,
TN 37831-6269
E. E. Hoffman
Deputy Assistant Manager for Energy Research and Development
- 115-124. DOE, OFFICE OF SCIENTIFIC AND TECHNICAL INFORMATION,
P.O. Box 62, Oak Ridge, TN 37831
(For distribution by microfiche as shown in DOE/OSTI-4500,
Distribution Category UC-330 (Transportation Systems),
UC-103 (Fluidized Bed Combustion), UC-109 (Goal Gasification
(Surface and Underground), and UC-114 (Coal-Based Instrumentation)